

A novel conjunction filter based on the minimum distance between perturbed trajectories

A.S. Rivero¹, G. Baù², R. Vazquez³, and C. Bombardelli⁴

^{1,3}Department of Aerospace Engineering, Universidad de Sevilla

²Department of Mathematics, Università di Pisa

⁴Department of Applied Physics, Universidad Politécnica de Madrid

Abstract

The increasing congestion in the near-Earth space environment has amplified the need for robust and efficient conjunction analysis techniques including the computation of the minimum distance between orbital paths in the presence of perturbations. After showing that classical Minimum Orbit Intersection Distance (MOID) computation schemes are unsuitable to treat Earth orbiting objects, the article presents an analytical approach to provide a more accurate estimate of the true distance between perturbed trajectories by incorporating the effect of zonal harmonics of arbitrary order. Cook's linear secular theory for the motion of the eccentricity vector is extended to include higher order eccentricity effects and applied to the computation of the minimum and maximum radii attained by two orbits at their mutual nodes, which can be employed to estimate the true distance between the two orbital paths and to establish an efficient algorithm for determining or excluding potential conjunctions. Extensive testing and validation are conducted using a high-fidelity propagator and a comprehensive dataset of resident space objects. The results demonstrate an accuracy below the km level for the orbit distance computation in 99% of cases, which enables high-efficiency conjunction filtering.

1 Introduction

The near-Earth space environment is undergoing a profound transformation in the “new space era” [Muelhaupt et al., 2019] characterized by a significant surge in space traffic, the deployment of extensive satellite constellations, and the escalating proliferation of space debris. This evolution presents increasingly formidable challenges for space management, particularly concerning the safety and sustainability of space operations. Conjunction Analysis (CA) emerges as a pivotal tool in this context, offering methodologies and processes to evaluate and mitigate collision risks in orbit. By combining advanced detection techniques, risk assessment, and collision avoidance decision-making, CA plays a crucial role in safeguarding space assets and ensuring the long-term sustainability of the space environment [Kerr and Sánchez Ortiz, 2021].

At present, operators, space agencies, and providers of Space Situational Awareness (SSA) and Space Surveillance and Tracking (SST) services are primarily focused on addressing what is known as the *one-vs-all* conjunction screening problem [Kerr and Sánchez Ortiz, 2021]. This entails a meticulous scrutiny of

potential conjunctions between one single active satellite and the extensive catalog of space objects. While this empowers operators to make well-informed decisions regarding Collision Avoidance Maneuvers (CAM) to protect their assets, it falls short in addressing the myriad of unexplored collisions among the rest of the catalogued RSO population. These collisions pose a significant threat, potentially leading to the formation of hazardous fragment clouds capable of causing substantial damage or even the complete loss of operational satellites. Achieving a comprehensive understanding of the near-Earth space environment necessitates considering conjunctions among all conceivable combinations of cataloged objects, commonly referred to as the *all-vs-all* scenario [Stevenson et al., 2023]. However, implementing this broader perspective presents formidable computational challenges due to the ever-increasing number of potential conjunction pairs.

Previous research endeavors have sought solutions to these challenges through the exploration of diverse filtering processes [Woodburn et al., 2010, Escobar et al., 2012, Casanova et al., 2014, Rivero et al., 2024] and the utilization of parallel computing techniques [Healy, 1995]. Typically, a sequence of three filters is applied in cascade starting from an apogee-perigee filter [recently improved taking into account the effect of zonal harmonics in Rivero et al., 2024] followed by an orbit path filter and a time filter [see Hoots et al., 1984, Casanova et al., 2014]. An alternative approach in which the apogee-perigee filter is followed by a different set of “sieves” has also been proposed [Alarcón Rodríguez et al., 2002]. The application of filters to eliminate pairs of Resident Space Objects (RSOs) with no collision risk has emerged as one of the most widely adopted techniques for expediting computational processes in conjunction analyses.

The widely adopted *orbit path filter*, which is the main focus of the present work, hinges on the distance between two trajectories irrespective of the actual position of the two objects along them. A pair of objects whose orbits have a mutual distance above a safe and carefully established threshold have a negligible probability of collision and can thus be eliminated (i.e., filtered out) from further computation.

For Keplerian orbits, the function of the distance between two orbits has been thoroughly investigated in the literature [Gronchi, 2003, 2005, Hedo et al., 2018, 2020, Gronchi et al., 2023]. The absolute minimum of that function, known as the Minimum Orbit Intersection Distance or MOID, is of great importance in astronomy and widely employed to assess the collision risk between astronomical bodies. In principle, a Keplerian MOID computation scheme can be applied to perturbed orbits by considering osculating orbital elements. However, as it will be shown in the present work, the corresponding “osculating” MOID function falls short from providing a good estimation of the true distance (i.e., the “true” MOID) between RSO pairs in low-Earth orbit. This aspect was already noticed by the works of Hoots et al. [1984] and Woodburn et al. [2010] where the applicability of purely Keplerian modeling for the implementation of path filters was shown to be problematic.

In order to address these challenges and increase the robustness of the orbit path filter, different approaches have been proposed in the literature. Numerical iteration and sampling taking into account J_2 -induced orbital plane precession have been proposed by Hoots et al. [1984] and Woodburn et al. [2010] in order to adapt an orbit path filter to the effect of environmental perturbations. In spite of these efforts, Woodburn et al. [2010] conclude by not recommending the use of a path filter, which is labelled as “troublesome”. Alfano [2012] introduces a geometrical approach, offering versatility by enabling users to specify different in-plane and out-of-plane bounds for the path filter. However, in order to fully eliminate false negatives, relatively large buffer distances (above 30 km) are incorporated.

The approach proposed in the present work, leading to the design of a “space occupancy path conjunction filter” (SOP-filter), is based on three fundamental ideas. The first is to avoid treating RSO pairs with mutual inclination outside of the range $[10, 170]$ degrees and orbit eccentricities exceeding 0.1. The former condition ensures that the MOID falls in the vicinity of the line of intersection between the two orbit planes,

the latter allows us an analytical treatment of the problem. As shown in the results section, and taking the current space catalogue, pairs not satisfying these conditions (and that will clearly remain unfiltered) amount to about 5% of total number of pairs analysed by the new filter. The second idea is to estimate for each object of a given pair the orbit radius at the mutual nodes using an efficient analytical approach based on the extension of the work by Rivero et al. [2024], which incorporates a complete zonal gravitational perturbation model and considers this effect over a selected conjunction screening timeframe. The third idea is to estimate for each of the two mutual nodes the minimum and maximum values taken by the orbit radius across a typical 5-days conjunction, thus defining for each object two radial intervals, and check whether the intervals relative to the same pair of mutual nodes overlap. If no overlap is detected the pair can be filtered out.

The article’s structure is as follows. Section 2 introduces the definition of true MOID between perturbed orbit paths and points out the inadequacy of a Keplerian MOID function to estimate this quantity. Section 3 is devoted to the computation of an analytical expression for the evolution of the orbit radius under the effect of a complete zonal perturbation model. It provides a generalization of a similar expression obtained by Rivero et al. [2024] by including higher order eccentricity effects that are crucial for the correct implementation of the newly proposed filter and the influence of all even zonal harmonics by following the theory of Cook [1992]. Subsequently, Section 4 delineates the development and analytical implementation of a new orbit path filter based on the short-term SO model. Then, Section 5 offers an analysis of the filter’s performance, focusing on reliability and effectiveness. These results are corroborated using a high-fidelity propagator. The article concludes with some final remarks in Section 6.

2 True vs. Keplerian osculating MOID

The implementation of an effective orbit path filter relies on the concept of minimum orbit intersection distance (MOID) between two, generally non-Keplerian trajectories T_A and T_B . Rigorously, that distance is the minimum distance between any two of their respective points P_A and P_B and will be referred here as true MOID:

$$\text{true MOID} = \min_{P_A \in T_A, P_B \in T_B} \|P_A - P_B\|.$$

The preceding quantity can be estimated by considering all possible pairs of points on the numerically propagated trajectories and selecting the pair with minimum distance. If the two trajectories are sampled with sufficient spatial resolution that estimation can be taken as an accurate value for their true MOID.

In order to save computational time, one might want to consider computing the MOID of the two osculating Keplerian trajectories at different instants of time by employing their osculating orbital elements and exploiting high efficiency MOID computation tools available in the literature [e.g., Gronchi et al., 2023]. In doing this, one ends up with a Keplerian osculating MOID as a function of time and can consider the minimum of that function as a proxy for the true MOID [see for instance Alfano, 2012, Casanova et al., 2014, Bonaccorsi et al., 2024]. Unfortunately, as it will be shown in the following examples, the minimum of the Keplerian osculating MOID is generally not a good estimate for the true MOID.

Fig. 1 shows the evolution of the Keplerian osculating MOID function computed at each integration time step for different orbit pairs (the initial conditions are reported in Table 1) and using a high-fidelity dynamical model. As it is evident, in both cases the osculating MOID function goes to zero repeatedly. However, the numerically estimated true MOID for the two cases yields values that are far from zero (22.97 km and 9.58 km, respectively). These examples suggest that Keplerian MOID functions are unsuitable for

RSO (NORAD)	41732	42775	41460
a (km)	6,839.44	6,867.10	6,875.36
e	0.0023	0.0019	0.0125
i (deg)	97.36	97.20	98.27
ω (deg)	120.14	139.31	129.61
Ω (deg)	229.73	339.11	129.53

Table 1: Osculating orbital elements at epoch JD 2,459,885.88 for the RSOs considered in Fig. 1.

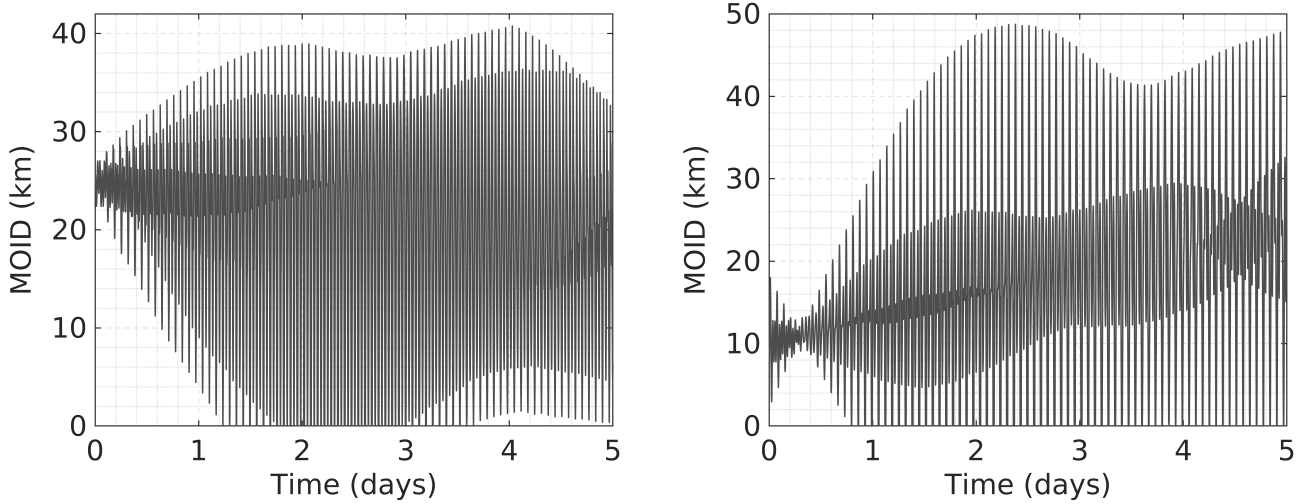


Figure 1: Keplerian osculating MOID for the two pairs of objects NORAD 41732, NORAD 42775 (left) and NORAD 41732, NORAD 41460 (right).

the implementation of an efficient path filter and that a non-Keplerian approach should be developed instead. It is anticipated that the method developed in this work estimates a minimum distance of 22.92 km and 8.57 km for the two preceding test cases.

3 Analytical expression of the orbit radius

In a previous work [Rivero et al., 2024] related to the implementation of a space occupancy filter (SO-filter), an analytical expression for the evolution of the orbit radius was obtained as

$$r \simeq \hat{a} (1 - \hat{e} \cos(\hat{\theta} - \hat{\omega})) + \frac{J_2}{4\hat{a}} [(9 + \cos 2\hat{\theta}) \sin^2 \hat{i} - 6], \quad (1)$$

where $J_2 \approx 1.082 \times 10^{-3}$ is the second Earth gravitational harmonic, and \hat{e} , $\hat{\omega}$, \hat{a} , \hat{i} , and $\hat{\theta}$ represent the mean values (averaged over the mean anomaly) of the eccentricity, argument of perigee, semi-major axis, inclination, and argument of latitude, respectively. The analytical expressions of \hat{e} , $\hat{\omega}$ employed in Rivero et al. [2024] are based on the 1966 theory developed by Graham E. Cook [Cook, 1966], which accounts for a zonal model with J_2 plus an arbitrary number of odd zonal terms while \hat{a} and \hat{i} are kept constant.

Equation (1) is simple enough to allow a fully analytical implementation of an SO filter through the

solution of a quartic equation and provides sufficient accuracy to compute the critical points of the orbit radius as required in this work (see Section 4.2).

However, a more refined expression for both the orbit radius and the different mean orbital elements appearing in equation (1) is necessary for an accurate implementation of the orbit path filter proposed here and will be dealt with in the following.

3.1 Expression of the orbit radius including higher order eccentricity terms

This section focuses on finding an approximation of the orbit radius evolution with time that generalises equation (1) by including higher order effects in the mean eccentricity. As done in Rivero et al. [2024], the analytical expression for the radius is derived by accounting for short-period effects depending linearly on the J_2 zonal harmonic term and neglecting the influence of higher order harmonics. However, in order to make the formulation applicable up to moderate eccentricities ($\hat{e} < 0.1$), the next expansions are considered up to order 3 in the eccentricity.

By using a classical result [see Smart, 1953], the orbit radius can be approximated as

$$r \simeq a \left[1 - e \cos M + \frac{1}{2}e^2(1 - \cos 2M) + \frac{3}{8}e^3(\cos M - \cos 3M) \right].$$

Each orbital element a , e , and M is replaced in the formula above with the sum of its mean (\hat{a} , \hat{e} , \hat{M}) and short-periodic (a_s , e_s , M_s) variation. The expressions of a_s , e_s , M_s derived by Kozai [1959] and Lyddane [1963] can be written as

$$a_s = \mathbf{a}_s + J_2 O(\hat{e}), \quad e_s = \mathbf{e}_s + J_2 O(\hat{e}), \quad \hat{e}M_s = \mathbf{m}_s + J_2 O(\hat{e}),$$

where

$$\mathbf{a}_s = \frac{3\kappa J_2}{2\hat{a}} \cos(2\hat{\nu} + 2\hat{\omega}), \quad (2)$$

$$\mathbf{e}_s = \frac{J_2}{8\hat{a}^2} [7\kappa \cos(3\hat{\nu} + 2\hat{\omega}) + 6(2 - 3\kappa) \cos \hat{\nu} + 3\kappa \cos(\hat{\nu} + 2\hat{\omega})], \quad (3)$$

$$\mathbf{m}_s = \frac{J_2}{8\hat{a}^2} [-7\kappa \sin(3\hat{\nu} + 2\hat{\omega}) - 6(2 - 3\kappa) \sin \hat{\nu} + 3\kappa \sin(\hat{\nu} + 2\hat{\omega})], \quad (4)$$

with $\hat{\nu}$, $\hat{\omega}$ the mean values of the true anomaly and argument of perigee, respectively, $\kappa = \sin^2 \hat{i}$, and \hat{i} is the mean inclination. Then, by applying the following approximation:

$$\cos(jM) \simeq \cos(j\hat{M}) - jM_s \sin(j\hat{M}), \quad j = 1, 2, 3,$$

the orbit radius is given by

$$\begin{aligned} r \simeq & (\hat{a} + a_s) \left(1 - (\hat{e} + e_s)(\cos \hat{M} - M_s \sin \hat{M}) \right. \\ & + \frac{1}{2}(\hat{e} + e_s)^2 (1 - \cos 2\hat{M} + 2M_s \sin 2\hat{M}) \\ & \left. + \frac{3}{8}(\hat{e} + e_s)^3 [\cos \hat{M} - M_s(\sin \hat{M} - 3 \sin 3\hat{M}) - \cos 3\hat{M}] \right). \end{aligned}$$

Neglecting the terms that contain $J_2 \hat{e}^n$, with $n \geq 1$, yields

$$r \simeq \hat{a} + \alpha_s - \hat{a} \left[(\hat{e} + \mathbf{e}_s) \cos \hat{M} - m_s \sin \hat{M} - \frac{1}{2} \hat{e}^2 (1 - \cos 2\hat{M}) - \frac{3}{8} \hat{e}^3 (\cos \hat{M} - \cos 3\hat{M}) \right]. \quad (5)$$

Finally, through the equation of the center [see Smart, 1953], one can write

$$\hat{M} = \hat{\nu} - 2\hat{e} \sin \hat{\nu} + \frac{3}{4} \hat{e}^2 \sin 2\hat{\nu} - \frac{1}{3} \hat{e}^3 \sin 3\hat{\nu} + O(\hat{e}^4),$$

so that

$$\cos \hat{M} = \cos \hat{\nu} + 2\hat{e} \sin^2 \hat{\nu} - \frac{7}{2} \hat{e}^2 \cos \hat{\nu} \sin^2 \hat{\nu} + O(\hat{e}^3), \quad (6)$$

$$\cos 2\hat{M} = \cos 2\hat{\nu} + 8\hat{e} \cos \hat{\nu} \sin^2 \hat{\nu} + O(\hat{e}^2). \quad (7)$$

Using (2), (3), (4), (6), and (7) in equation (5), the final expression of the orbit radius becomes

$$r \simeq \hat{a} (1 - \hat{e} \cos(\hat{\theta} - \hat{\omega})) \left(1 - \hat{e}^2 \sin^2(\hat{\theta} - \hat{\omega}) \right) + \frac{J_2}{4\hat{a}} \left[(9 + \cos 2\hat{\theta}) \sin^2 \hat{i} - 6 \right], \quad (8)$$

where the mean argument of latitude $\hat{\theta} = \hat{\nu} + \hat{\omega}$ has been introduced.

In equation (8) the quantities \hat{a} , \hat{i} are assumed to be constant, while $\hat{\theta}$, \hat{e} , $\hat{\omega}$ vary with time. The evolutions of \hat{e} , $\hat{\omega}$ are obtained from an extension of Graham E. Cook's theory developed in the next section.

3.2 Evolution of the eccentricity vector

The theory formulated by Graham E. Cook [see Cook, 1966] analytically describes the motion of the eccentricity vector under the effect of J_2 and an arbitrary number of odd zonal harmonics on orbits of small eccentricity. Richard A. Cook, in his 1992 paper [Cook, 1992], expands upon this result by including the impact of the remaining even harmonics by means of the inclination and eccentricity functions introduced by Kaula [1966]. Although the latter theory represents an improvement of the former, it still needs to be extended in order to be fully applicable to the implementation of the proposed orbit path filter. The extension involves the inclusion of higher order eccentricity terms.

In the following, the theory of Richard A. Cook is briefly summarized for the reader's convenience before developing the required eccentricity extension. For this purpose, Legendre polynomials are employed as in Cook [1966]. Let us adopt dimensionless units of length and time, taking the Earth radius, R_\oplus , as the reference length and $1/n_\oplus$ as the reference time, with n_\oplus indicating the mean motion of a Keplerian circular orbit of radius R_\oplus .

The differential equations describing the evolution of the mean eccentricity vector nodal components

$$\xi = \hat{e} \cos \hat{\omega}, \quad \eta = \hat{e} \sin \hat{\omega} \quad (9)$$

are

$$\begin{cases} \dot{\xi} = -k_\xi \eta + C, \\ \dot{\eta} = k_\eta \xi, \end{cases} \quad (10)$$

where k_ξ and k_η encompass the contribution due to the even harmonics up to the first order in the eccentricity and are defined by

$$\begin{aligned}
k_\xi &= - \sum_{n=1}^N J_{2n} \hat{n} \left(\frac{R_\oplus}{\hat{a}} \right)^{2n} \left(\frac{2n(2n+1)}{2} P_{2n}(\cos \hat{i}) P_{2n}(0) \right. \\
&\quad + \frac{(2n-1)(2n-2)(2n-2)!}{2(2n+2)!} P_{2n}^2(\cos \hat{i}) P_{2n}^2(0) \\
&\quad \left. - P'_{2n}(\cos \hat{i}) P_{2n}(0) \cot \hat{i} \right), \\
k_\eta &= \sum_{n=1}^N J_{2n} \hat{n} \left(\frac{R_\oplus}{\hat{a}} \right)^{2n} \left(-\frac{2n(2n+1)}{2} P_{2n}(\cos \hat{i}) P_{2n}(0) \right. \\
&\quad + \frac{(2n-1)(2n-2)(2n-2)!}{2(2n+2)!} P_{2n}^2(\cos \hat{i}) P_{2n}^2(0) \\
&\quad \left. + P'_{2n}(\cos \hat{i}) P_{2n}(0) \cot \hat{i} \right),
\end{aligned}$$

with J_{2n} denoting the even zonal coefficient of degree $2n$.

The contribution to $\dot{\xi}$, $\dot{\eta}$ due to the odd harmonics up to the first order in the eccentricity appears in the constant term C , which is given by

$$C = \sum_{n=1}^N J_{2n+1} \hat{n} \left(\frac{R_\oplus}{\hat{a}} \right)^{2n+1} \frac{n}{(2n+1)(n+1)} P_{2n+1}^1(\cos \hat{i}) P_{2n+1}^1(0),$$

where J_{2n+1} represents the odd zonal coefficient of degree $2n+1$, P_n is the Legendre polynomial of degree n , P'_n its derivative with respect to the inclination, and P_n^s the associated Legendre function of order s and degree n . The solution of system (10) is given by

$$\begin{cases} \xi(\tau) = e_p \cos \left(k_\xi \sqrt{\frac{k_\eta}{k_\xi}} \tau + \alpha \right), \\ \eta(\tau) = \sqrt{\frac{k_\eta}{k_\xi}} e_p \sin \left(k_\xi \sqrt{\frac{k_\eta}{k_\xi}} \tau + \alpha \right) + e_f, \end{cases} \quad (11)$$

where τ denotes the non-dimensional time. The additional term e_f , known as *frozen eccentricity*, is defined by

$$e_f = \frac{C}{k_\xi}.$$

Moreover, the amplitude e_p , which is known as *proper eccentricity*, and the phase α depend on the initial conditions of the eccentricity and argument of perigee:

$$\begin{aligned}
e_p &= \sqrt{\hat{e}_0^2 \cos^2 \hat{\omega}_0 + \frac{k_\xi}{k_\eta} (\hat{e}_0 \sin \hat{\omega}_0 - e_f)^2}, \\
\cos \alpha &= \frac{\hat{e}_0 \cos \hat{\omega}_0}{e_p}, \quad \sin \alpha = \sqrt{\frac{k_\xi}{k_\eta}} \left(\frac{\hat{e}_0 \sin \hat{\omega}_0 - e_f}{e_p} \right).
\end{aligned}$$

Solution (11) corresponds to an ellipse of semiaxis $e_p \sqrt{k_\eta/k_\xi}$ along the η axis and semiaxis e_p along the ξ axis. Typically, the semi-major axis of this ellipse aligns with the η -axis, except for orbits with inclinations very close to the critical value.

3.2.1 Including $J_2 \hat{e}^2$ terms

Both Graham and Richard Cook's analytical solutions neglect the effect of nonlinear terms in the eccentricity. As it will be shown in the following, the most important nonlinear terms are of the order of $J_2 \hat{e}^2$ and influence the phasing of the mean eccentricity vector rotation in such a way that they cannot be neglected when evaluating the distance between two orbits. A clarifying example of this is summarized in Fig. 2, which illustrates the evolution of the errors in the mean eccentricity vector nodal components made by R. Cook's solution over one precession period of the apsidal line for the catalogued object NORAD 29740. The initial conditions, taken from the TLEs at epoch 2022 November 2, 16:22:53, correspond to an initial eccentricity of ≈ 0.1 . While the amplitudes of oscillation of ξ and η are well-reproduced by R. Cook's theory as compared to the numerical (averaged) solution, the frequencies are smaller.

In order to improve the analytical solution, the contributions due to the J_2 up to the third-order in the eccentricity are retained in the expressions of $\dot{\xi}$, $\dot{\eta}$. After replacing U' in equations (3) and (4) of Cook [1966] with the Earth's gravitational potential associated to the second harmonic averaged over one orbit [see Battin, 1999]

$$U_2 = J_2 (\hat{n} R_\oplus)^2 \left(\frac{1}{2} - \frac{3}{4} \sin^2 \hat{i} \right) (1 - \hat{e}^2)^{-3/2},$$

where $\hat{n} = \sqrt{\mu/\hat{a}^3}$, and applying the aforementioned approximation, one has

$$\begin{cases} \dot{\xi} = - [k_\xi + 2k(\xi^2 + \eta^2)] \eta + C, \\ \dot{\eta} = [k_\eta + 2k(\xi^2 + \eta^2)] \xi, \end{cases}$$

where

$$k = 3J_2 \hat{n} \left(\frac{R_\oplus}{\hat{a}} \right)^2 \left(1 - \frac{5}{4} \sin^2 \hat{i} \right).$$

These equations cannot be solved analytically. However, by assuming that the squared eccentricity term $\xi^2 + \eta^2$ is constant and equal to its initial value $\hat{e}_0^2 = \xi^2(0) + \eta^2(0)$, the system becomes linear:

$$\begin{cases} \dot{\xi} = -\kappa_\xi \eta + C, \\ \dot{\eta} = \kappa_\eta \xi, \end{cases} \quad (12)$$

where

$$\begin{aligned} \kappa_\xi &= k_\xi + 2k\hat{e}_0^2, \\ \kappa_\eta &= k_\eta + 2k\hat{e}_0^2. \end{aligned}$$

The proposed approximation is reasonable considering that the time interval of interest in this work is 5 days, while the mean value of the period of the line of apsides is typically around 150 days. The solution

of system (12) can be expressed in the same form as in (11), wherein k_ξ and k_η are replaced by κ_ξ and κ_η , respectively:

$$\begin{cases} \xi(\tau) = e_p \cos\left(\kappa_\xi \sqrt{\frac{\kappa_\eta}{\kappa_\xi}} \tau + \alpha\right), \\ \eta(\tau) = \sqrt{\frac{\kappa_\eta}{\kappa_\xi}} e_p \sin\left(\kappa_\xi \sqrt{\frac{\kappa_\eta}{\kappa_\xi}} \tau + \alpha\right) + e_f. \end{cases} \quad (13)$$

The evolution of the errors in the mean eccentricity vector nodal components obtained using the third-order correction (13) is displayed in Fig. 2 with the grey dashed line. The new proposed solution closely approximates the numerical one.

3.3 Expression of the orbit radius including the evolution of the eccentricity vector

Let us define the quantity

$$\beta = \kappa_\xi \sqrt{\frac{\kappa_\eta}{\kappa_\xi}} \tau + \alpha, \quad (14)$$

which appears in solution (13). This angle shows a *slow* evolution as opposed to the *fast* angle $\hat{\theta}$ which was previously introduced in the expression (8) of the orbit radius. Over a time interval of 5 days, $\hat{\theta}$ varies cyclically in the range $[0, 2\pi)$ several times, while β covers only a limited arc. This significant difference in time scales allows us to assume β and $\hat{\theta}$ to be independent. Then, the orbital distance can be considered as a function of β and $\hat{\theta}$. The expression of $r(\hat{\theta}, \beta)$ is obtained from (8) by first using the definitions of ξ and η given in (9) and then solution (13):

$$\begin{aligned} r \simeq & \hat{a} \left(1 - e_p \cos \beta \cos \hat{\theta} - \sqrt{\frac{\kappa_\eta}{\kappa_\xi}} e_p \sin \beta \sin \hat{\theta} - e_f \sin \hat{\theta} \right) \cdot \\ & \left[1 - \left(e_p \cos \beta \sin \hat{\theta} - \sqrt{\frac{\kappa_\eta}{\kappa_\xi}} e_p \sin \beta \cos \hat{\theta} - e_f \cos \hat{\theta} \right)^2 \right] \\ & + \frac{J_2}{4\hat{a}} \left[(9 + \cos 2\hat{\theta}) \sin^2 \hat{\theta} - 6 \right]. \end{aligned} \quad (15)$$

4 The orbit path filter

This section describes the algorithm developed for the orbit path filter, which is formulated as an optimization problem. For each object of a given pair, the proposed procedure estimates the minimum and maximum values of the orbit radius among those attained in a given time interval $[t_0, t_f]$ when the object is located at the mutual nodes. From the two minima and two maxima, relative to the two mutual nodes, a filtering criterion is formulated.

The absolute minimum and maximum of the orbit radius $r(\hat{\theta}, \beta)$ are searched in two compact domains

$$\mathcal{D} = \mathcal{T} \times \mathcal{B}, \quad \mathcal{D}^* = \mathcal{T}^* \times \mathcal{B} \quad (16)$$

as described in Section 4.2. The interval for the variable β is

$$\mathcal{B} = [\beta_{\min}, \beta_{\max}],$$

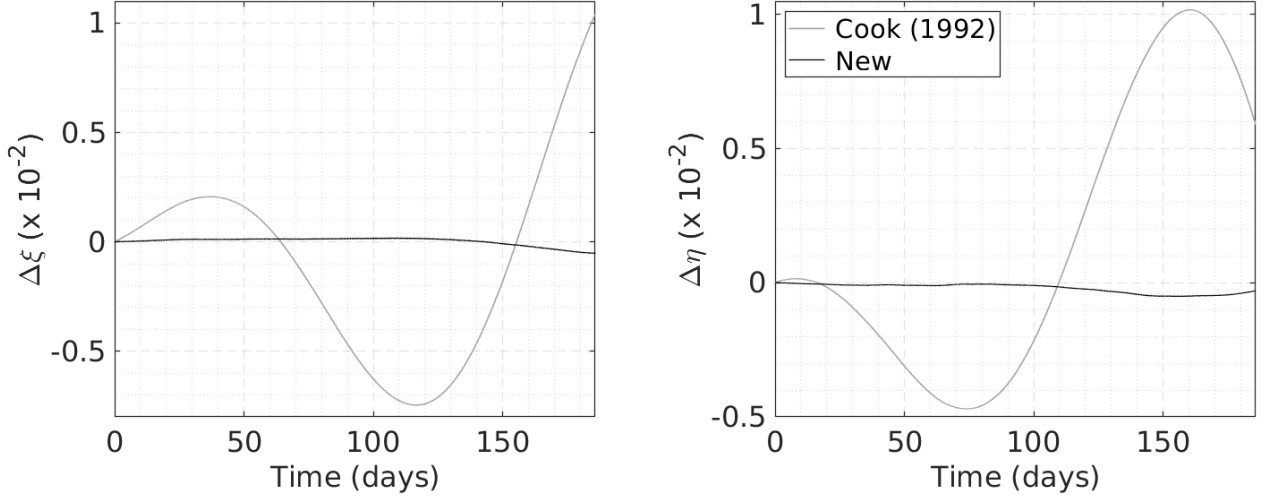


Figure 2: Evolution of the errors in the mean eccentricity vector nodal components computed from Cook [1992] and the improved theory leading to solution (13).

where the extrema β_{\min} , β_{\max} are given by setting $\tau = t_0, t_f$, respectively, in (14). The computation of the domains \mathcal{T} , \mathcal{T}^* for the variable $\hat{\theta}$ is described in Section 4.1. It is based on the assumption that if the mutual inclination between the orbital planes of the two objects is sufficiently large, the MOID is achieved by two points that are close to one pair of mutual nodes [Gronchi, 2003].

In Section 4.3 it is explained how the filter employs the minimum and maximum values of the orbit radius in each of the two domains \mathcal{D} , \mathcal{D}^* and for each of the two objects under consideration to evaluate whether a possible conjunction event could occur between them in $[t_0, t_f]$.

4.1 Computation of the intervals \mathcal{T} , \mathcal{T}^*

The location of the mutual nodes is predicted by taking into account the influence of the geopotential on the longitudes of the nodes. In particular, the secular effect due to the zonal harmonics J_2 , J_3 , J_4 derived in Kozai [1962] has been implemented for the time evolution of $\hat{\Omega}$.

For convenience, all orbits are considered direct (i.e., $\hat{i} \in [0, \pi/2]$). If $\hat{i} > \pi/2$, then \hat{i} is replaced by $\pi - \hat{i}$ and $\hat{\Omega}$ by $\pi + \hat{\Omega} \pmod{2\pi}$. Moreover, it is not restrictive to assume that $\hat{i}_1 > \hat{i}_2$. The latitude of one of the two pairs of mutual nodes is given by¹ (see Fig. 3)

$$\phi = \arcsin \left(\frac{\sin \hat{i}_1 \sin \hat{i}_2 \sin \Delta \hat{\Omega}}{\sin \gamma} \right),$$

where \hat{i}_1, \hat{i}_2 are the mean inclinations of the two orbital planes, $\Delta \hat{\Omega} = \hat{\Omega}_2 - \hat{\Omega}_1$, and the mutual inclination γ , which is defined as the angle between the directions orthogonal to the orbital planes, is found from relation

$$\gamma = \arccos \left(\cos \hat{i}_1 \cos \hat{i}_2 + \sin \hat{i}_1 \sin \hat{i}_2 \cos \Delta \hat{\Omega} \right).$$

¹The latitude of the other pair is equal to $-\phi$.

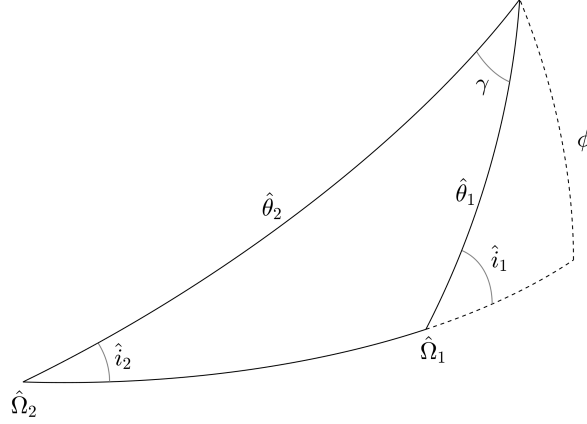


Figure 3: Spherical triangles generated from the ascending nodes and one pair of mutual nodes of two trajectories. The mutual inclination γ is also indicated.

If $\hat{i}_1 \hat{i}_2 \neq 0$, the arguments of latitude of the mutual nodes are computed from

$$\sin \hat{\theta}_k = \frac{\sin \phi}{\sin \hat{i}_k}, \quad k = 1, 2, \quad (17)$$

which admits two solutions in $[0, 2\pi]$. The ambiguity can be solved by looking at the projection of the orbit over a non-rotating Earth in the inertial reference frame, here named *trace*. The relative displacement of the traces of two (non-coplanar) ellipses as $\Delta\hat{\Omega}$ is varied in the range $[0, 2\pi]$ is shown in Fig. 4. The motion along the traces occurs from left to right. The curve labelled “Trace 1” refers to the same trajectory in the four scenarios, which is given by $\hat{a}_1 = 7,300$ km, $\hat{e}_1 = 0.002$, $\hat{i}_1 = 75$ deg, $\hat{\omega}_1 = 90$ deg, $\hat{\Omega}_1 = 0$ deg. The curve “Trace 2” refers to the trajectory defined by $\hat{a}_2 = 7,800$ km, $\hat{e}_2 = 0.008$, $\hat{i}_2 = 35$ deg, $\hat{\omega}_2 = 0$ deg, while $\hat{\Omega}_2$ takes four different values. The third trace (“Trace 2 shifted”) displayed in Fig. 4 is generated from the same trajectory relative to Trace 2 by changing $\hat{\Omega}_2$ of a small amount. Note that the value $\hat{\Omega}_1 = 0$ is chosen only for convenience and the following analysis is valid for any value of $\hat{\Omega}_1$.

Four particular configurations can be identified: the mutual nodes lie on the equatorial plane ($\phi = 0$), so that either $\Delta\hat{\Omega} = 0$ (Fig. 4a) or $\Delta\hat{\Omega} = \pi$ (Fig. 4c); the latitudes of the two pairs of mutual nodes are equal to the maximum and minimum latitudes reached along “Trace 2” ($\phi = \pm\hat{i}_2$, see Figs. 4b and 4d). The latter condition is realized by two values of $\Delta\hat{\Omega}$ which are computed as follows. Consider the configuration shown in Fig. 5, which refers to Fig. 4d, and in particular to the intersection point between “Trace 1” and “Trace 2” with the smaller right ascension. Noting that $\phi = \hat{i}_2$ and $\hat{\theta}_2 = \pi/2$, the argument of latitude of the mutual node along the trajectory of Trace 1 is given by

$$\hat{\theta}_1^* = \arcsin \left(\frac{\sin \hat{i}_2}{\sin \hat{i}_1} \right), \quad (18)$$

and the value taken by $\hat{\Omega}_1 - \hat{\Omega}_2 \pmod{2\pi}$, here denoted by α , is computed from the formula

$$\alpha = \frac{\pi}{2} - \arctan (\tan \hat{\theta}_1^* \cos \hat{i}_1). \quad (19)$$

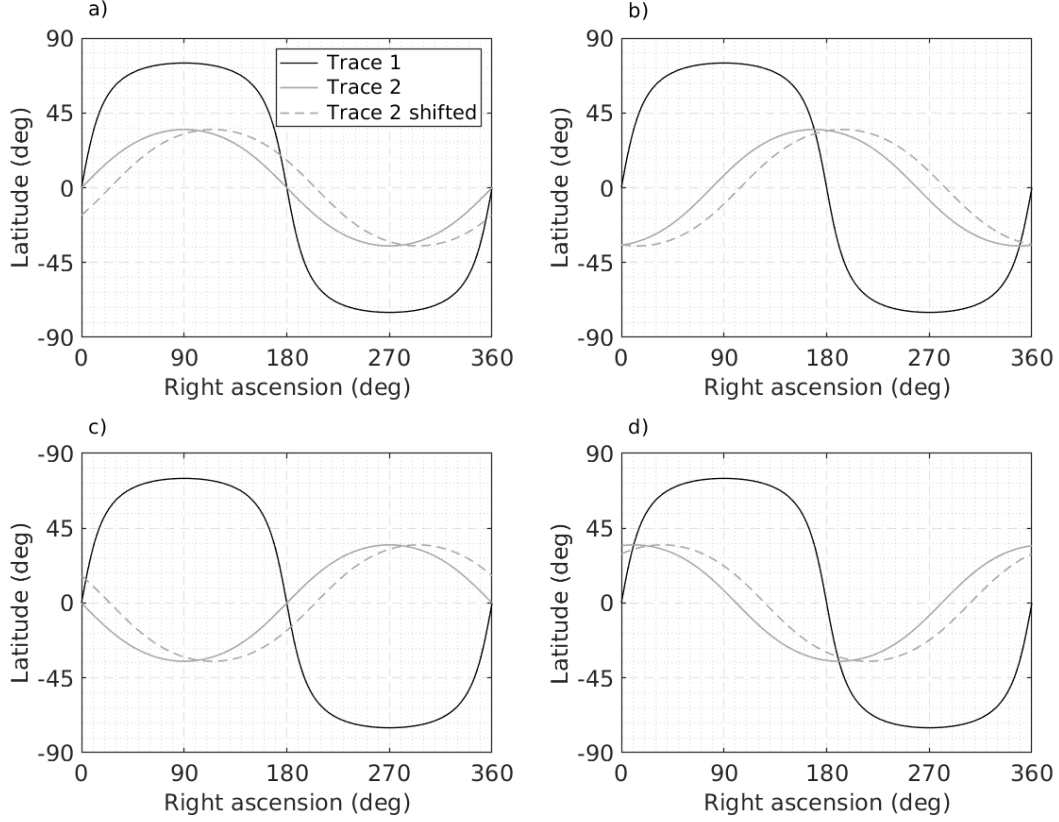


Figure 4: Orbital traces (“Trace 1” and “Trace 2”) of two ellipses (their orbital elements are specified in the text) in four different configurations: a) $\Delta\hat{\Omega} = 0$, b) $\Delta\hat{\Omega} = \alpha$, c) $\Delta\hat{\Omega} = \pi$, d) $\Delta\hat{\Omega} = 2\pi - \alpha$, where $\Delta\hat{\Omega} = \hat{\Omega}_2 - \hat{\Omega}_1$ and α is defined in equation (19). “Trace 2 shifted” is obtained by adding $5\pi/36$ to $\hat{\Omega}_2$.

Then, it results $\Delta\hat{\Omega} = 2\pi - \alpha$. In a similar way, it is possible to see that the configuration of traces 1 and 2 in Fig. 4b is realized by $\Delta\hat{\Omega} = \alpha$, with α and $\hat{\theta}_1^*$ still defined as in (19) and (18).

Therefore, as $\Delta\hat{\Omega}$ is increased from 0 to 2π , one realizes through Fig. 4 that the arguments of latitude of the pair of mutual nodes in the Northern hemisphere (i.e., $\phi \in [0, \pi/2]$) belong to the intervals reported in Table 2.

In the time span $[t_0, t_f]$ the quantity $\Delta\hat{\Omega}$ varies monotonically from

$$\Delta\hat{\Omega}_0 = \hat{\Omega}_2(t_0) - \hat{\Omega}_1(t_0)$$

to

$$\Delta\hat{\Omega}_f = \hat{\Omega}_2(t_f) - \hat{\Omega}_1(t_f),$$

where, the final values $\hat{\Omega}_1(t_f), \hat{\Omega}_2(t_f)$ will differ by a few degrees from the initial ones, since $t_f = 5$ days. Let us restrict $\Delta\hat{\Omega}_0, \Delta\hat{\Omega}_f$ to $[0, 2\pi]$ and introduce

$$I_{\Omega} = \begin{cases} [\Delta\hat{\Omega}_0, \Delta\hat{\Omega}_f] & \text{if } \Delta\hat{\Omega}_f > \Delta\hat{\Omega}_0, \\ [\Delta\hat{\Omega}_0, 2\pi) \cup [0, \Delta\hat{\Omega}_f] & \text{if } \Delta\hat{\Omega}_0 > \Delta\hat{\Omega}_f. \end{cases}$$

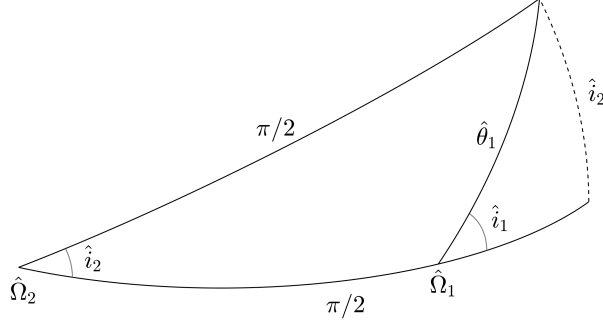


Figure 5: Spherical triangles generated from the ascending nodes and one pair of mutual nodes of two trajectories in the particular case $\phi = \hat{i}_2$.

$\Delta\hat{\Omega}$	$\hat{\theta}_1$	$\hat{\theta}_2$
$I_a = [0, \alpha]$	$[\pi/2, \pi]$	$[\pi/2, \pi]$
$I_b = [\alpha, \pi]$	$[\pi/2, \pi]$	$[0, \pi/2]$
$I_c = [\pi, 2\pi - \alpha]$	$[0, \pi/2]$	$[\pi/2, \pi]$
$I_d = [2\pi - \alpha, 2\pi]$	$[0, \pi/2]$	$[0, \pi/2]$

Table 2: Ranges of the arguments of latitude of the pair of mutual nodes in the Northern hemisphere as $\Delta\hat{\Omega}$ varies in $[0, 2\pi]$.

There are three different cases to discuss.

If $I_\Omega \subset I_k$, $k \in \{a, b, c, d\}$, where the intervals I_k are defined in Table 2, the arguments of latitude of the pair of mutual nodes in the Northern hemisphere vary monotonically for $\tau \in [t_0, t_f]$. Then, one can set

$$\begin{aligned}\hat{\theta}_{\min,k} &= \min(\hat{\theta}_k(t_0), \hat{\theta}_k(t_f)), \\ \hat{\theta}_{\max,k} &= \max(\hat{\theta}_k(t_0), \hat{\theta}_k(t_f)),\end{aligned}\tag{20}$$

where $\hat{\theta}_k(t_0)$, $\hat{\theta}_k(t_f)$ are computed through relation (17) with $\phi \in (0, \pi/2]$ and Table 2. The intervals \mathcal{T}_k , \mathcal{T}_k^* are given by

$$\begin{aligned}\mathcal{T}_k &= [\hat{\theta}_{\min,k}, \hat{\theta}_{\max,k}], \\ \mathcal{T}_k^* &= [\hat{\theta}_{\min,k} + \pi, \hat{\theta}_{\max,k} + \pi].\end{aligned}\tag{21}$$

If instead at some time \bar{t} the latitudes of the mutual nodes reach the maximum (\hat{i}_2) and minimum ($-\hat{i}_2$) values, that is, $\alpha \in I_\Omega$ or $2\pi - \alpha \in I_\Omega$, then the time derivative of $\hat{\theta}_1$ will vanish at \bar{t} . Thus, $\hat{\theta}_1$ will increase in $[t_0, \bar{t})$ and decrease in $(\bar{t}, t_f]$, while $\hat{\theta}_2$ will vary monotonically. As a consequence, $\hat{\theta}_{\min,2}$, $\hat{\theta}_{\max,2}$ can be

computed from (20), and

$$\begin{cases} \hat{\theta}_{\min,1} = \pi - \hat{\theta}_1^* & \text{if } \alpha \in I_\Omega, \\ \hat{\theta}_{\max,1} = \hat{\theta}_1^* & \text{if } 2\pi - \alpha \in I_\Omega, \end{cases} \quad (22)$$

where $\hat{\theta}_1^*$ is defined in (18). Moreover, $\hat{\theta}_{\max,1}$ (if $\alpha \in I_\Omega$), $\hat{\theta}_{\min,1}$ (if $2\pi - \alpha \in I_\Omega$) are given by (20). Also in this case $\mathcal{T}_k, \mathcal{T}_k^*$ are defined as shown in (21).

Finally, if the two pairs of mutual nodes cross the equatorial plane, that is, if $0 \in I_\Omega$ or $\pi \in I_\Omega$, the arguments of latitude of the mutual nodes vary monotonically for $\tau \in [t_0, t_f]$. In this case, the intervals for $\hat{\theta}$ result

$$\begin{aligned} \mathcal{T}_k &= [\hat{\theta}_{\max,k} + \pi, 2\pi) \cup [0, \hat{\theta}_{\min,k}], \\ \mathcal{T}_k^* &= [\hat{\theta}_{\max,k}, \hat{\theta}_{\min,k} + \pi], \end{aligned} \quad (23)$$

where, for each object, $\hat{\theta}_{\min,k}, \hat{\theta}_{\max,k}$ are computed from (20).

The intervals $\mathcal{T}_k, \mathcal{T}_k^*$ can be inflated through the application of an *angular buffer* (see Section 5.3.1).

4.2 Orbit radius bounds

This section presents an efficient method for determining the minimum and maximum values taken by the orbit radius $r(\hat{\theta}, \beta)$ (see 15) at the mutual nodes in each domain $\mathcal{D}, \mathcal{D}^*$ (see 16).²

First, the critical points of the function $r(\hat{\theta}, \beta)$ are computed on its domain of definition $[0, 2\pi] \times \mathbb{R}$. Since their computation would considerably slow down the SOP-filter, a simpler approach is adopted³. Four critical points can be easily found: $(\pi/2, \pi/2), (\pi/2, 3\pi/2), (3\pi/2, \pi/2), (3\pi/2, 3\pi/2)$. Additional critical points to these four can appear only if the frozen and proper eccentricities, and accordingly $\hat{e},$ are $\ll 1$. By neglecting the nonlinear terms in the eccentricity in the expression of r given in (15), the resulting function still admits the four critical points reported above and allows for an explicit computation of the additional critical points when they exist as described in Rivero et al. [2024], where Graham Cook's theory is employed (i.e., $\kappa_\xi = \kappa_\eta$). The corresponding critical values of r are always calculated using equation (15).

If an absolute minimum/maximum point belongs to $\mathcal{D} (\mathcal{D}^*)$, then, the corresponding value of r is computed through equation (15). Otherwise, one has to search for the minimum/maximum of r on the border of $\mathcal{D} (\mathcal{D}^*)$ through the procedure described in Section 4.2.1, check whether there are local minimum/maximum points of r that belong to $\mathcal{D} (\mathcal{D}^*)$, and in this case, select the smallest/largest value of r .

Let $r_{\min,k}, r_{\max,k}$ and $r_{\min,k}^*, r_{\max,k}^*$ be the minimum and maximum orbit radii in the domains \mathcal{D}_k and \mathcal{D}_k^* , respectively, where $k = 1, 2$ refers to an object of the pair.

²In this section, the subscript $k = 1, 2$ which refers to the two objects of the considered pair is dropped to simplify the exposition.

³The critical points of $r(\hat{\theta}, \beta)$ are solutions of a system of two equations, each involving a bivariate trigonometric polynomial, which can be transformed to an ordinary polynomial by a change of variables. Then, by resultant theory [Cox et al., 1992] a univariate polynomial can be obtained such that all its roots represent one component of all the solutions of the system made by the two ordinary polynomials. In our case, the degree of such polynomial is 72 and the computation of its coefficients and its roots requires a complex procedure.

4.2.1 Bounds of the orbit radius on the border of \mathcal{D} and \mathcal{D}^*

Let us denote by $\partial\mathcal{D}$, $\partial\mathcal{D}^*$ the borders of \mathcal{D} , \mathcal{D}^* , respectively, and introduce the functions

$$\begin{aligned} r_{\beta_*}(\hat{\theta}) &= r(\hat{\theta}, \beta_*), \\ r_{\hat{\theta}_*}(\beta) &= r(\hat{\theta}_*, \beta), \end{aligned}$$

where $r(\hat{\theta}, \beta_*)$, $r(\hat{\theta}_*, \beta)$ are two trigonometric polynomials obtained from $r(\theta, \beta)$ in (15) by replacing β , $\hat{\theta}$ with some constants β_* , $\hat{\theta}_*$, respectively. For both $\partial\mathcal{D}$ and $\partial\mathcal{D}^*$ one has to take $\beta_* = \beta_{\min}, \beta_{\max}$. Moreover, for $\partial\mathcal{D}$, either $\hat{\theta}_* = \hat{\theta}_{\min}, \hat{\theta}_{\max}$ (see 21) or $\hat{\theta}_* = \hat{\theta}_{\min} + \pi, \hat{\theta}_{\max} + \pi$ (see 23) and for $\partial\mathcal{D}^*$, either $\hat{\theta}_* = \hat{\theta}_{\min} + \pi, \hat{\theta}_{\max} + \pi$ (see 21) or $\hat{\theta}_* = \hat{\theta}_{\max}, \hat{\theta}_{\min} + \pi$ (see 23). A point $(\hat{\theta}_*, \beta_*)$ defines a *vertex* of the domain.

The critical points of $r_{\beta_*}(\hat{\theta})$, $r_{\hat{\theta}_*}(\beta)$ are solutions of the equations

$$\frac{dr_{\beta_*}}{d\hat{\theta}} = 0, \quad \frac{dr_{\hat{\theta}_*}}{d\beta} = 0, \quad (24)$$

where

$$\frac{dr_{\beta_*}}{d\hat{\theta}} = B_0 + \sin \hat{\theta} \sum_{m=0}^2 S_m \sin^m \hat{\theta} + \cos \hat{\theta} \sum_{m=0}^2 C_m \sin^m \hat{\theta},$$

for some coefficients $B_0(\beta_*)$, $S_m(\beta_*)$, $C_m(\beta_*)$, and

$$\frac{dr_{\hat{\theta}_*}}{d\beta} = b_0 + \sin \beta \sum_{m=0}^2 s_m \sin^m \beta + \cos \beta \sum_{m=0}^2 c_m \sin^m \beta,$$

for some coefficients $b_0(\hat{\theta}_*)$, $s_m(\hat{\theta}_*)$, $c_m(\hat{\theta}_*)$. Using relations

$$\begin{aligned} \sin \hat{\theta} &= \frac{2x}{1+x^2}, & \cos \hat{\theta} &= \frac{1-x^2}{1+x^2}, \\ \sin \beta &= \frac{2y}{1+y^2}, & \cos \beta &= \frac{1-y^2}{1+y^2}, \end{aligned}$$

equations (24) can be transformed in two equations involving the ordinary polynomials

$$q(x) = \sum_{n=0}^6 q_n x^n = 0, \quad p(y) = \sum_{n=0}^6 p_n y^n = 0, \quad (25)$$

where the coefficients $q_n(\beta_*)$, $p_n(\hat{\theta}_*)$ are provided in Appendix A. For each real root \bar{x} of $q(x)$ there exists a unique critical point of r_{β_*} , given by

$$\hat{\theta}^c = 2 \arctan \bar{x} \pmod{2\pi}.$$

Instead, for each real root \bar{y} of $p(y)$ there exist infinite critical points of $r_{\hat{\theta}_*}$, given by

$$\beta_h^c = 2 \arctan \bar{y} + 2h\pi, \quad h \in \mathbb{Z}.$$

Consider $\partial\mathcal{D}$, the following discussion being the same for $\partial\mathcal{D}^*$. If for the values of β_* and $\hat{\theta}_*$ that define $\partial\mathcal{D}$, none of the points $(\hat{\theta}^c, \beta_*)$, $(\hat{\theta}_*, \beta_h^c)$ lie on $\partial\mathcal{D}$, then necessarily the minimum and maximum of r on $\partial\mathcal{D}$ are reached at two vertices of \mathcal{D} . Otherwise, one has to find the smallest and largest values of r among those (if any) computed at the vertices of \mathcal{D} and at the points $(\hat{\theta}_h^c, \beta_*)$, $(\hat{\theta}^*, \beta^c)$ that lie on $\partial\mathcal{D}$.

Finally, if either $\pi \in \mathcal{T}$ or $\pi \in \mathcal{B}$, the values of the orbit radius at the points on $\partial\mathcal{D}$ with $\hat{\theta} = \pi$ or $\beta = \pi$ are compared with the minimum and maximum orbit radii found by the procedure described above.

4.3 Filter output

Consider a pair of space objects and introduce the following intervals ($k = 1, 2$):

$$\mathcal{R}_k = [r_{\min,k}, r_{\max,k}], \quad \mathcal{R}_k^* = [r_{\min,k}^*, r_{\max,k}^*].$$

If

$$\mathcal{R}_1 \cap \mathcal{R}_2 = \emptyset \quad \wedge \quad \mathcal{R}_1^* \cap \mathcal{R}_2^* = \emptyset, \quad (26)$$

the pair is flagged as *negative* and is not considered for further investigation, as a conjunction between the two objects is deemed impossible. Otherwise, if

$$\mathcal{R}_1 \cap \mathcal{R}_2 \neq \emptyset \quad \vee \quad \mathcal{R}_1^* \cap \mathcal{R}_2^* \neq \emptyset, \quad (27)$$

it is flagged as *positive*, thus requiring more in-depth analysis.

The intervals \mathcal{R}_k , \mathcal{R}_k^* can be enlarged through the application of a *radial buffer* (see Section 5.3.2).

5 Results

The SOP-filter algorithm, developed in Section 4, has been tested and validated using the same dataset as well as the same high-fidelity dynamical model employed in Rivero et al. [2024]. From the publicly available Two-Line Element sets (TLEs), 16,951 orbits were extracted and then processed using the SGP4 theory [Vallado et al., 2006]. The dataset is obtained by removing orbits with an eccentricity higher than 0.1 and an apogee radius exceeding 40,000 km. Moreover, orbits with inclinations smaller than 0.06 deg are also excluded (21 orbits from the sample).

The dynamical model includes a 23×23 geopotential along with luni-solar third-body perturbations, and it accounts for Earth's geoid precession, nutation, and polar motion effects. Earth orientation, the values of the harmonic coefficients, and the positions of the Sun and Moon are obtained from the corresponding SPICE kernels. Note that the SOP-filter is based on a model where only the zonal harmonics are taken into account and Earth's polar axis is aligned with the z -axis of the J2000 inertial frame.

The orbits of the dataset were propagated to a common epoch t_0 (11/02/2022, 09:18:20) and then processed by these two filters in sequence: the SO-filter developed in Rivero et al. [2024] and the SOP-filter proposed in this work. The time window $t_f - t_0$ was set equal to 5 days. The SO-filter passes 32,474,006 out of the 143,659,725 input pairs. The SOP-filter is applied only to the pairs with a mutual inclination in the range $[10, 170]$ deg. Pairs not satisfying this condition amount to 1,637,190 (about 5%) and are flagged as positive, thus requiring further analysis. The remaining 30,836,816 pairs are processed by the SOP-filter. Table 3 summarises some information about the numerical test. In particular, it reports the *real* number of

input orbits	16,951
almost coplanar pairs	1,637,190
input pairs	30,836,816
positive pairs	6,452,412

Table 3: SOP-filter input orbits and pairs. The pairs that could potentially generate a collision are denoted as “positive pairs”.

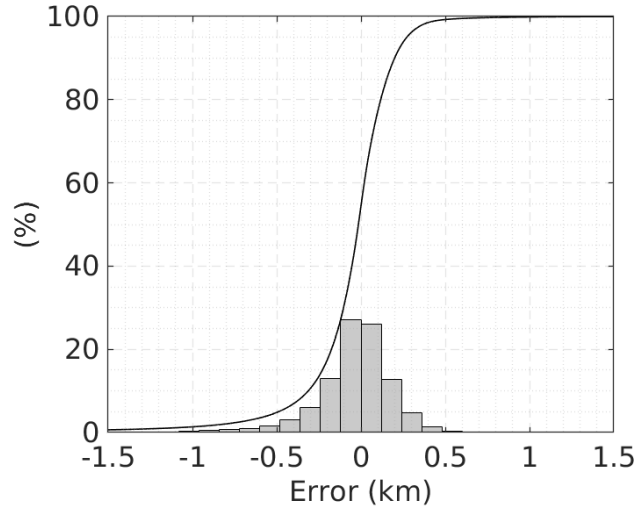


Figure 6: Histogram and cumulative density function of the errors in the minimum and maximum values of orbit radius inside the domains \mathcal{D} , \mathcal{D}^* (see Section 4.2) for the input pairs of the SOP-filter. A negligible percentage of errors is outside the interval $[-1.5, 1.5]$ km.

pairs that could potentially generate a collision according to condition (27), as computed from numerical propagations.

Before describing the results of the SOP-filter, the accuracy in the computation of the bounds of the orbit radius (see Section 4.2) is assessed. For each of the 30,836,816 pairs, the values of $r_{\min,k}$, $r_{\max,k}$, $r_{\min,k}^*$, $r_{\max,k}^*$ ($k = 1, 2$) obtained from the analytical procedure are compared to those obtained from numerical propagations with the high-fidelity dynamical model. In particular, a positive error means that the estimated maximum/minimum orbit radius is smaller/larger than the numerical value. Fig. 6 illustrates the distribution and cumulative density function of the set made by all these errors (eight values for each pair), revealing a mean error margin close to 0. Notably, 99% of the examined cases displayed an error smaller than 0.39 km, underscoring the robustness of the algorithm. Moreover, the maximum error is about 4.40 km. Additionally, Fig. 7 displays the same set of errors of Fig. 6 against the eccentricity. The larger is this orbital element, the higher are the errors in the minimum and maximum values of the orbit radii.

The performance of the SOP-filter is assessed through the metrics introduced in Section 5.1. Next, the results obtained without applying any buffer are presented in Sections 5.2. Finally, the analysis of the angular and radial buffers and the results obtained by applying these buffers are presented in Sections 5.3 and 5.4.

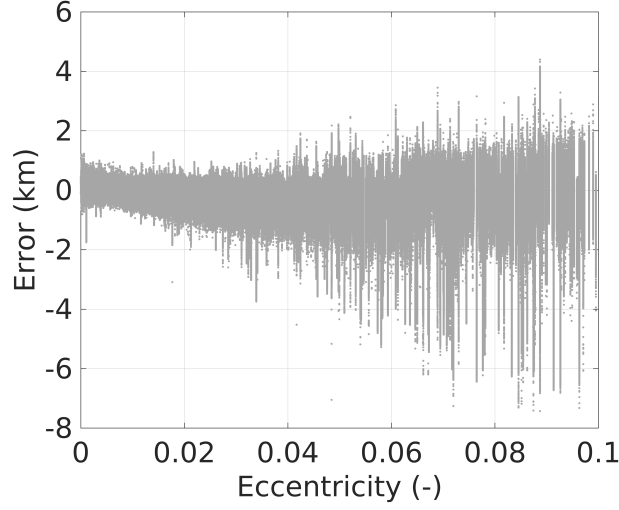


Figure 7: Same errors used to obtain Fig. 6 versus the eccentricity \hat{e} .

5.1 Performance metrics

The following two definitions are relevant to evaluate the performance of the SOP-filter.

A *false positive* occurs when the filter evaluates a pair as positive because condition (27) is satisfied, while the pair is flagged as negative from the result of the numerical propagation. A *false negative* occurs when the filter evaluates a pair as negative because condition (26) is satisfied, while the pair is flagged as positive from the result of the numerical propagation. Usually, one wants to minimize or possibly reduce to zero the number of false negatives, without increasing too much the number of false positives.

In order to evaluate the amount of false positives and false negatives three different metrics are employed, following Rivero et al. [2024].

The *false positives to true positives* ratio is defined as

$$\rho_{fp} = \frac{N_{fp}}{N_{tp}}, \quad (28)$$

where N_{fp} and N_{tp} are the numbers of false and true positives, respectively.

The *false negatives to true positives* ratio is defined as

$$\rho_{fn} = \frac{N_{fn}}{N_{tp}},$$

where N_{fn} is the number of false negatives.

Finally, the *filter effectiveness* is

$$\eta = \frac{N_{out}}{N}, \quad (29)$$

where N_{out} is the number of pairs eliminated by the filter because they are flagged as negative and therefore can not generate a collision, and N is the total number of pairs over which the filter is tested, that is 30,836,816.

false positives	46,609
false negatives	439,873
ρ_{fp}	0.775 %
ρ_{fn}	7.316 %
η	80.351 %

Table 4: SOP-filter performance without buffers.

5.2 SOP-filter results without buffers

Consider first the case where the angular and radial buffers are not applied. This means that for any pair the intervals $\mathcal{T}_k, \mathcal{T}_k^*$ and $\mathcal{R}_k, \mathcal{R}_k^*$ are computed as described in Sections 4.1 and 4.2, 4.3, respectively, and they are not inflated.

Table 4 outlines the results of the SOP-filter, including the number of false positives and false negatives, along with the three previously defined metrics. The filter eliminates about 80.35% of the total number of pairs. However, there are too many false negatives, amounting to about 6.82% of the real number of positive pairs reported in Table 3. This serious issue is addressed here by introducing the angular and radial buffers.

5.3 Buffers analysis

Errors affecting the accuracy of the SOP-filter arise mainly from the location of the mutual nodes and the computation of the orbit radius. To mitigate these errors and avoid false negatives, the intervals $\mathcal{T}_k, \mathcal{T}_k^*$ and $\mathcal{R}_k, \mathcal{R}_k^*$ are enlarged by means of an angular and radial buffer, respectively. This approach, while is effective in eliminating false negatives, might cause a considerable increase in false positives if the chosen buffers become too large.

The two sources of error are analyzed in Sections 5.3.1 and 5.3.2.

5.3.1 Angular buffer

For each pair of objects, the intervals $\mathcal{T}_k, \mathcal{T}_k^*$ ($k = 1, 2$) are enlarged by subtracting and adding to the lower and higher endpoints, respectively, an angular shift. This quantity will be different for the two endpoints, and its computation is described below.

Consider the i -th pair, with $i \in [N] = \{1, \dots, N\}$. Let $\hat{\theta}_{k,i}(t_0), \hat{\theta}_{k,i}(t_f)$ and $\theta_{k,i}(t_0), \theta_{k,i}(t_f)$ be the arguments of latitude of the mutual nodes in the Northern hemisphere at the initial and final time computed as explained in Section 4.1 (i.e., $\hat{\theta}_k(t_0), \hat{\theta}_k(t_f)$) and by numerical propagations with the high-fidelity model, respectively. The following errors can be defined:

$$\begin{aligned}\epsilon_{k,i}(t_0) &= |\hat{\theta}_{k,i}(t_0) - \theta_{k,i}(t_0)|, \\ \epsilon_{k,i}(t_f) &= |\hat{\theta}_{k,i}(t_f) - \theta_{k,i}(t_f)|,\end{aligned}\tag{30}$$

with $k = 1, 2, i = 1, \dots, N$. Fig. 8 shows the distribution and cumulative density function of all the errors $\epsilon_{k,i}(t_0)$ (left plot) and $\epsilon_{k,i}(t_f)$ (right plot). Although the mean error in both plots is nearly 0, the errors at t_f display a greater dispersion as expected because of the approximate analytical prediction of $\hat{\Omega}_k(t_f)$. At t_0 , 99% of all errors are smaller than 0.062 deg, while at t_f , this value increases to 0.111 deg.

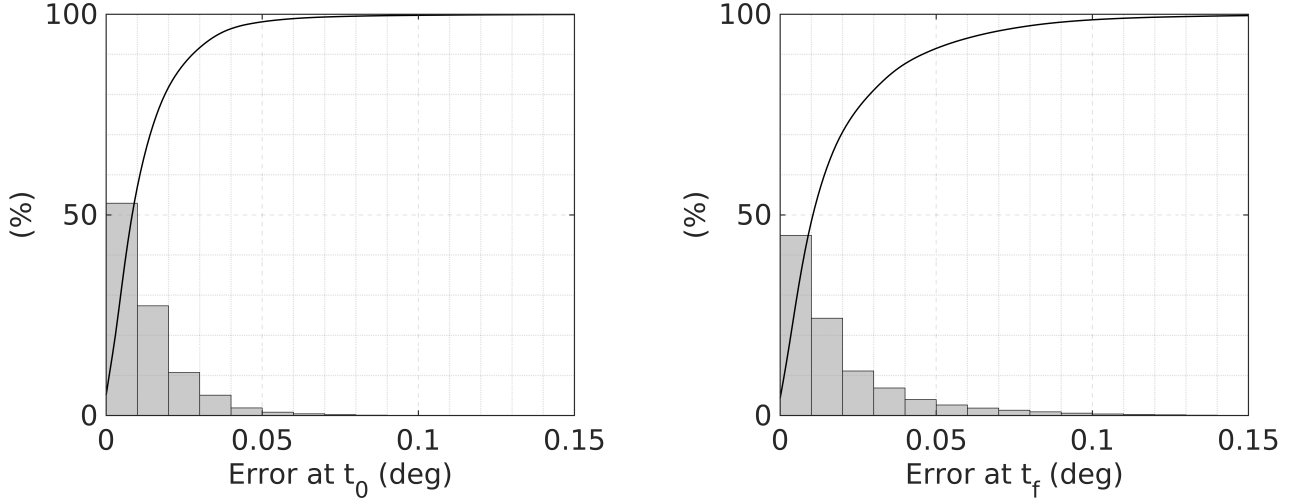


Figure 8: Histogram and cumulative density function of the errors in the argument of latitude of the mutual nodes in the Northern hemisphere at the initial (left) and final time (right) for the input pairs of the SOP-filter.

Figs. 9 and 10 represent the same errors of Fig. 8 (left) and Fig. 8 (right), respectively, versus the mutual inclination. In both figures, the color bar gives information on the orbit inclination. One can observe how the error increases as the mutual inclination approaches 10 deg and (even if less appreciably) 170 deg. Moreover, Fig. 10 shows that also small values of the inclination can lead to a loss of accuracy in the computation of the arguments of latitude of the mutual nodes at the final epoch t_f .

This analysis reveals that the largest errors can be explained considering the mutual and orbit inclinations. Therefore, angular buffers dependent on the values of these quantities (γ, \hat{i}) are introduced as follows. The domain $\mathcal{S} = [\gamma_0, \pi - \gamma_0] \times [0, \pi)$ of (γ, \hat{i}) , where $\gamma_0 = \pi/18$, is split into $n \times m$ equal subdomains

$$\mathcal{S}_{(u,v)} = \left\{ (\gamma, \hat{i}) : \gamma_0 + \frac{\pi - \gamma_0}{n}(u - 1) \leq \gamma \leq \gamma_0 + \frac{\pi - \gamma_0}{n}u, \right. \\ \left. \frac{\pi}{m}(v - 1) \leq \hat{i} < \frac{\pi}{m}v \right\},$$

with $u = 1, \dots, n, v = 1, \dots, m$. Let $\mathcal{F}_{(u,v)}$ be the subset of $\{1, 2\} \times [N]$ containing the pairs of indexes (k, i) corresponding to the object k of the i -th pair such that its mutual and orbit inclinations belong to $\mathcal{S}_{(u,v)}$. Then, the following angular buffers are introduced for $u = 1, \dots, n, v = 1, \dots, m$:

$$\delta_0(u, v) = \max_{(k,i) \in \mathcal{F}_{(u,v)}} \epsilon_{k,i}(t_0), \\ \delta_f(u, v) = \max_{(k,i) \in \mathcal{F}_{(u,v)}} \epsilon_{k,i}(t_f),$$

with $\epsilon_{k,i}(t_0), \epsilon_{k,i}(t_f)$ defined in (30). Appendix B reports the values of the angular buffers $\delta_0(u, v)$ and $\delta_f(u, v)$ for the different subdomains.

For each object of the input pairs (see Table 3), first one determines the values of the indexes u, v . Then, one subtracts from (adds to) the lower (higher) endpoints of \mathcal{T}_k and \mathcal{T}_k^* the angle $\delta_0(u, v)$ if the considered endpoint was computed from $\hat{\theta}(t_0)$, or the angle $\delta_f(u, v)$ if it was computed either from $\hat{\theta}(t_f)$ or from \hat{i}_1, \hat{i}_2 (see 22). In the latter case, which corresponds to the situation where the latitude of the mutual nodes

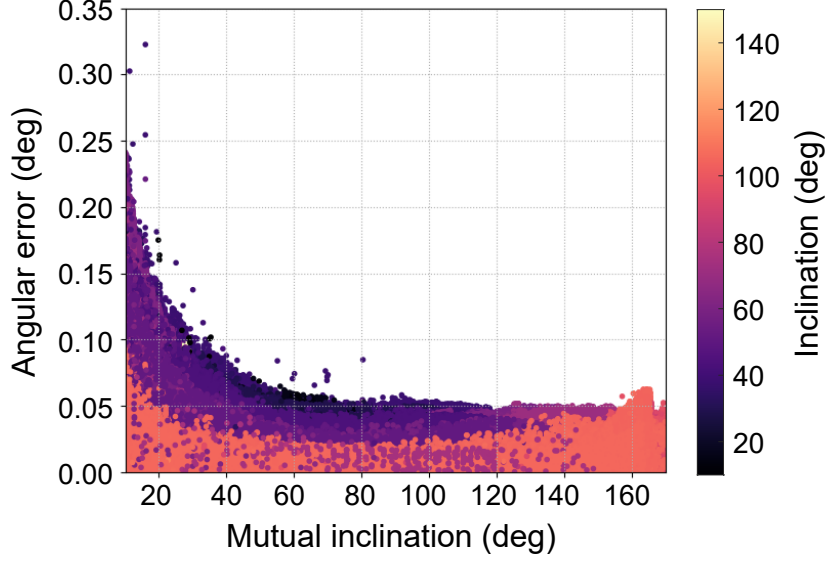


Figure 9: Errors in the argument of latitude of the mutual nodes in the Northern hemisphere at the initial time t_0 versus the mutual inclination γ for the input pairs of the SOP-filter. The color bar refers to the orbit inclination \hat{i} .

in the Northern hemisphere reaches its maximum value, this buffer is not optimal, however, only a small percentage of pairs falls in this case.

5.3.2 Radial buffer

The expression of the orbit radius employed by the SOP-filter is given in (15) as a function of β and $\hat{\theta}$, which are regarded as two independent variables. This assumption is motivated by the very separated time scales of their evolutions.

The accuracy of equation (15) is assessed by computing the values of r for $\hat{\theta} \in [0, 2\pi)$ and for $\tau \in [\tau_0, \tau_0 + T_C]$, where τ_0 is the initial epoch, fixed at 2,459,885.89 JD, and $T_C = 2\pi/\sqrt{\kappa_\xi \kappa_\eta}$ corresponds to one period of revolution of the apsidal line according to R. Cook's extended theory. Let $\beta_0, \beta_C = \beta_0 + \text{sgn } \kappa_\xi 2\pi$ be the values of β obtained from equation (14) with $\tau = \tau_0, \tau_0 + T_C$, respectively. The domain $[0, 2\pi) \times [\beta_0, \beta_C]$ for the variables $(\hat{\theta}, \beta)$ is sampled as follows

$$(\hat{\theta}_j, \beta_s) = \left(\frac{2\pi}{m}(j-1), \beta_0 + \text{sgn } \kappa_\xi \frac{2\pi}{m}s \right), \quad (j, s) \in \mathcal{G},$$

where $\mathcal{G} = \{(j, s) : 1 \leq j \leq m, 0 \leq s \leq m\}$. Let τ_s be the value of τ corresponding to β_s through equation (14).

Consider the n -th object, with $n \in [N_{\text{ob}}] = \{1, \dots, N_{\text{ob}}\}$ and N_{ob} is the number of input orbits (see Table 3). The following error can be defined:

$$\epsilon_n = \max_{(j,s) \in \mathcal{G}} |r_n(\hat{\theta}_j, \beta_s) - \mathbf{r}_n(\hat{\theta}_j; \tau_s)|, \quad (31)$$

where $r_n(\hat{\theta}, \beta)$ is the orbit radius computed from (15) and

$$\mathbf{r}_n(\hat{\theta}; \tau) = \frac{a_n(\tau)(1 - e_n(\tau)^2)}{1 + e_n(\tau) \cos(\hat{\theta} - \omega_n(\tau))},$$

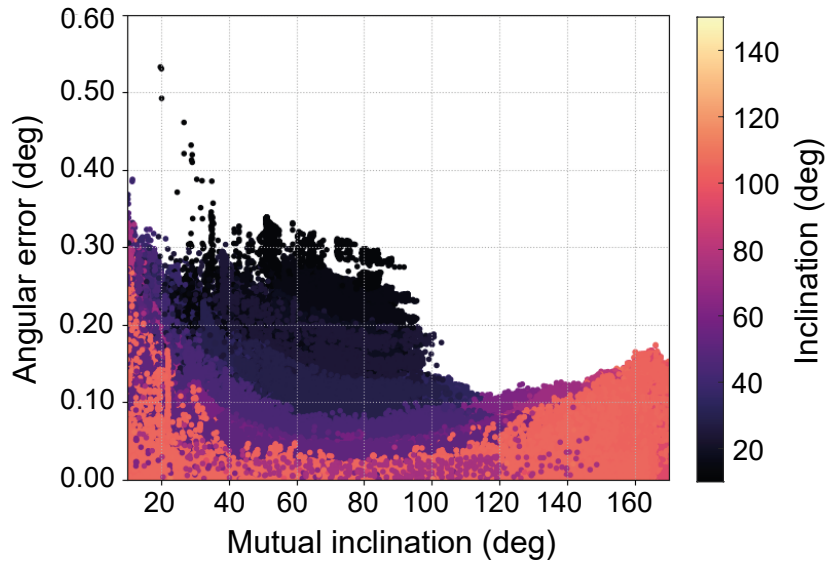


Figure 10: Same as in Fig. 9 but at the final time t_f .

with the osculating orbital elements a_n , e_n , and ω_n of the n -th object obtained by numerical propagation.

Fig. 11 depicts the distribution and cumulative density function of all the errors ϵ_n . The mean value of the distribution is about 0.5 km, and for 99% of the input objects the radial error is smaller than 1.55 km. On the other hand, the maximum error is much larger, amounting to about 4.88 km. Setting the radial buffer equal to this value would be too conservative for most of the orbits, and thus is far from being an optimal choice. A better approach is to adapt the size of the buffer based on those features of the orbits that impact the error.

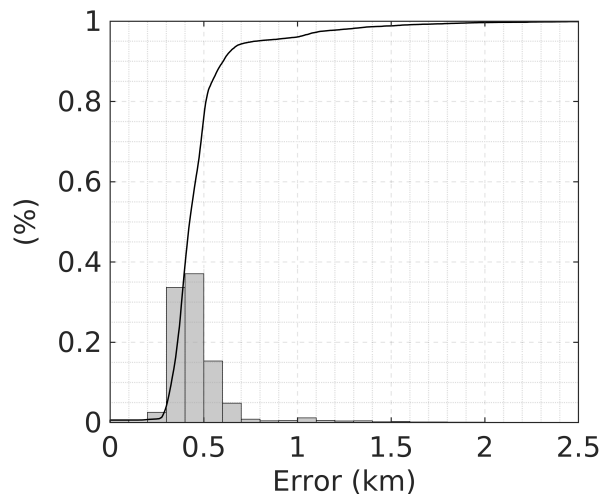


Figure 11: Histogram and cumulative density function of the radial error ϵ_n defined in (31) for the input objects of the SOP-filter.

It was shown in Fig. 7 that the eccentricity influences the error in the orbit radius. Here, Figs. 12 and 13

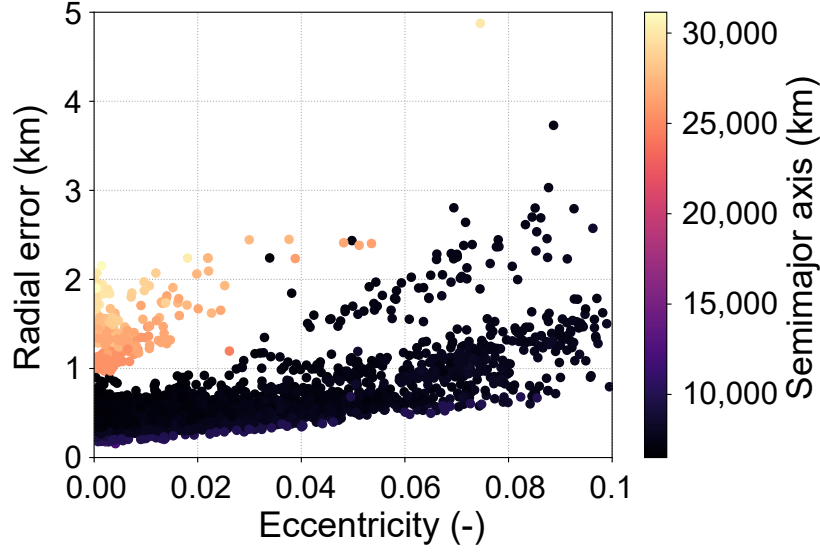


Figure 12: Radial error ϵ_n defined in (31) for the input objects of the SOP-filter versus the eccentricity \hat{e} . The color bar refers to the semi-major axis \hat{a} .

display the radial errors ϵ_n versus the eccentricity. The color bars denote the semi-major axis (Fig. 12) and the precession period T_C of the line of apsides (Fig. 13). From Fig. 12 it is evident that higher altitudes lead to larger errors. Indeed, equation (15) does not take into account third-body effects, which become more relevant as the semi-major axis increases. Notably, all orbits with eccentricities smaller than 0.02 and a radial error exceeding 1 km have a semi-major axis greater than 10,000 km. Concerning the influence of T_C , one can observe from Fig. 13 that for shorter precession periods, the increase of the error with the eccentricity is more pronounced. This is expected, since a smaller T_C implies a faster change in β , which instead is assumed fixed while $\hat{\theta}$ is varied in $[0, 2\pi)$.

In light of these results, the value of the radial buffer will depend on the semi-major axis (\hat{a}), eccentricity (\hat{e}), and period T_C . Following a similar procedure as in the previous section, the space $\hat{a} > 0$, $\hat{e} \in [0, 0.1]$, $T_C > 0$ is split into a finite number of subdomains. For each of them, the maximum of the errors ϵ_n (defined in equation 31) is computed over the indexes n of those objects whose mean orbital elements \hat{a} , \hat{e} , and period T_C belong to the considered subdomain. The resulting value defines the radial buffer of that subdomain.

For the k -th object ($k = 1, 2$) of the i -th pair ($i = 1, \dots, N$), the corresponding radial buffer is subtracted from (added to) the lower (higher) endpoints of both the radial intervals $\mathcal{R}_k, \mathcal{R}_k^*$. Appendix B reports the radial buffers of each subdomain.

5.4 SOP-filter results with buffers

The results of the SOP-filter with both the interval and radial buffers are presented. The former enlarge the domains $\mathcal{D}_k, \mathcal{D}_k^*$ where the minimum and maximum of the orbit radius of the object k of a given pair are searched for. The latter enlarges the intervals $\mathcal{R}_k, \mathcal{R}_k^*$ that are employed to decide whether a pair is positive or negative (see Section 4.3).

Table 5 summarises the outcomes obtained by applying the SOP-filter with the angular and radial buffers as detailed in Section 5.3. The filter excludes 75% of the input pairs from further conjunction assessment. Moreover, the number of pairs is reduced from 143,659,725 to 9,313,513 by the SO- and SOP-filters.

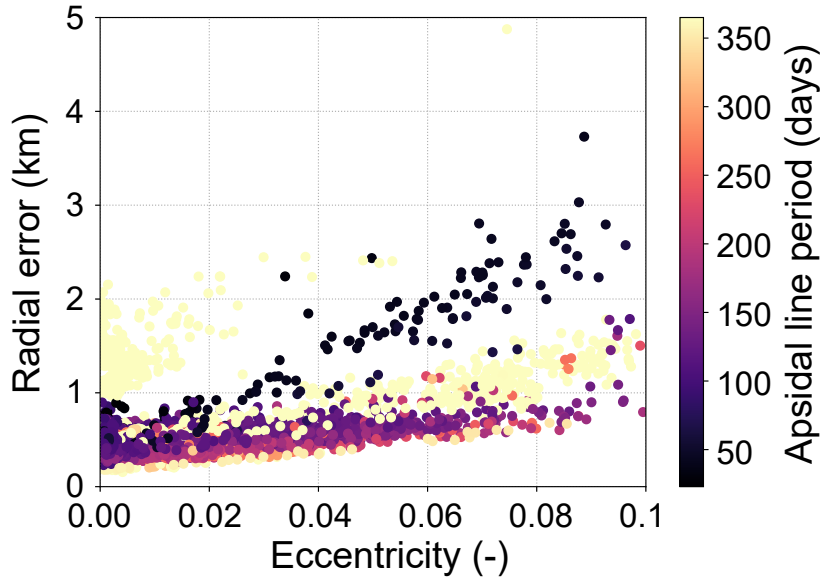


Figure 13: Same as in Fig. 12, but the color bar refers to the precession period of the apsidal line given by R. Cook’s extended theory.

false positives	1,223,911
false negatives	0
ρ_{fp}	18.968 %
η	75.107 %

Table 5: SOP-filter performance with buffers.

In conjunction analysis a safety distance D is commonly introduced to take into account of the uncertainty in the orbital state: a conjunction occurs if the distance between two objects is smaller than D . Different choices of D can be found in the literature [see for example Khutorovsky et al., 1993, Healy, 1995, Woodburn et al., 2010, Alfano, 2012, Casanova et al., 2014].

A threshold distance D is considered also in this work to further enlarge the intervals $\mathcal{R}_k, \mathcal{R}_k^*$. Fig. 14 shows how the SOP-filter’s performance metrics ρ_{fp} and η decrease as the distance D is increased from 0 to 4 km.

Comparing the proposed SOP-filter with similar methods existing in the literature is not an easy task. Here, a comparison is made with the filter sequence implemented by Casanova et al. [2014], where an *all vs. all* conjunction analysis of 864 objects is carried out. Their orbit path Filters I and II excluded 323,077 pairs, representing 86.7% of the total number of pairs. Notably, Filter I alone eliminated 41.1% of pairs, while Filter II further eliminated 77.2% of the remaining pairs. Employing the same threshold $D = 100$ m as in Casanova et al. [2014], the SOP-filter removed 74.95% of the pairs received from the SO-filter, which was able to exclude 77.40% of the input pairs. Therefore, the application of the SO- and SOP-filters reduced of 93.5% the number of pairs to be investigated, highlighting a considerable improvement.

Finally, computations were performed on a machine with an AMD EPYC 7542 32-Core Processor, with a base frequency of 1.5 GHz and max frequency of 2.9 GHz. The code was implemented in MATLAB R2021b,

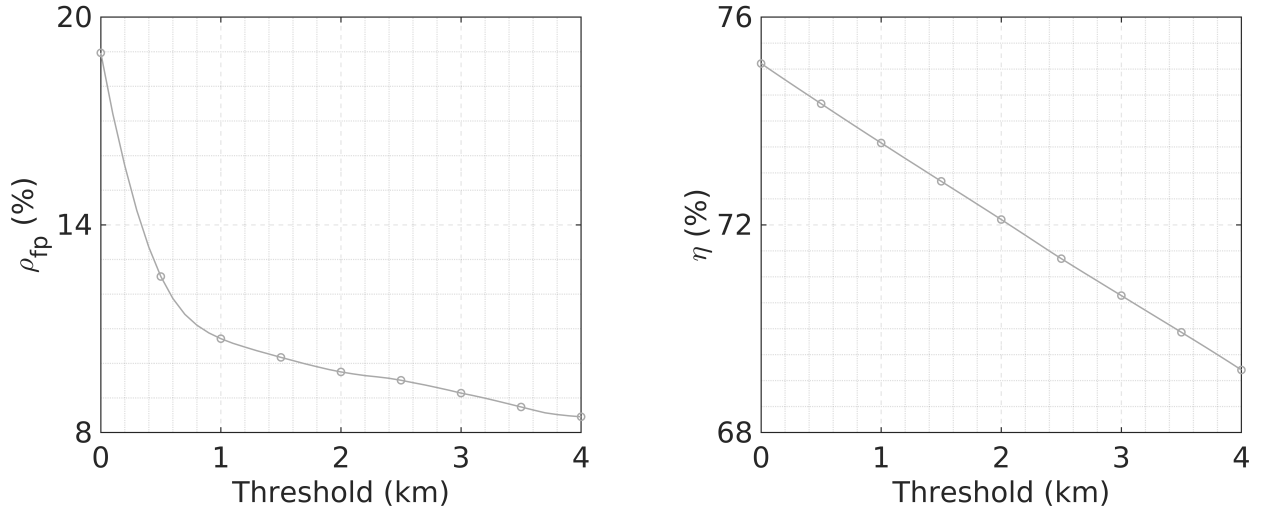


Figure 14: False positives to true positive ratio (left, see 28) and filter effectiveness (right, see 29) versus the applied threshold distance D .

utilizing the Parallel Computing Toolbox with 13 cores. With these specifications, the computational time required by the SOP-filter to process the 30,836,816 pairs was 4.07 hours.

6 Conclusions

The work introduces a novel approach for the estimation of the distance between perturbed orbital paths and for the implementation of an effective path filter to treat perturbed orbits in the Earth environment. The effect of environmental perturbations dominated by zonal harmonics is shown to play a key role in determining the true distance between orbital trajectories which makes the use of classical Keplerian MOID computation schemes unsuitable. In order to correctly incorporate these perturbations and treat orbits of small to moderate eccentricity (hence covering the great majority of resident space objects orbiting the Earth) an extension of the linear secular theory proposed by Cook (1966) is employed, which is an additional contribution of this work. An analytical procedure to estimate the upper and lower bound of radial distances at nodal crossings is derived accounting for short-period variations of the semi-major axis, eccentricity, and mean anomaly. In order to safely apply these analytical results to conjunction filtering and reduce false negatives to ideally zero, an angular and a radial buffer are implemented and carefully evaluated and tailored to the specific pair, thus avoiding an excessive growth of false positives. Extensive numerical tests show that the proposed filter is highly efficient, also in terms of computational time. After applying the filter to a dataset of 16,951 resident space objects, it eliminates 75.11% of the total pairs with no false negatives detected. Finally, when applied together with a previously developed space occupancy filter [see Rivero et al., 2024] 92.3% of the initial pairs are eliminated from further analysis. This dramatic reduction in the number of pairs has significant implications for space traffic management and collision risk mitigation.

Acknowledgements

A. S. Rivero and R. Vazquez gratefully acknowledge support by grant TED2021-132099B-C33 funded by MICIU/AEI/10.13039/501100011033 and by “European Union NextGenerationEU/PRTR”. Additionally, A. S. Rivero was funded by a FPU grant from the Spanish Ministry of Universities. G. Baù carried out this study within the Space It Up project funded by the Italian Space Agency, ASI, and the Ministry of University and Research, MUR, under contract n. 2024-5-E.0 - CUP n. I53D24000060005.

References

- J. R. Alarcón Rodríguez, F. M. Martínez Fadrique, and H. Klinkrad. Collision risk assessment with a “smart sieve” method. *European Space Agency, (Special Publication) ESA SP*, 486:159–164, 2002.
- S. Alfano. Toroidal path filter for orbital conjunction screening. *Celestial Mechanics and Dynamical Astronomy*, 113(3):321–334, 2012.
- R. H. Battin. *An Introduction to the Mathematics and Methods of Astrodynamics*. AIAA, Inc., 1999. p. 504.
- S. Bonaccorsi, M. F. Montaruli, P. Di Lizia, M. Peroni, A. Panico, M. Rigamonti, and F. Del Prete. Conjunction analysis software suite for space surveillance and tracking. *Aerospace*, 11(2), 2024.
- D. Casanova, C. Tardioli, and A. Lemaître. Space debris collision avoidance using a three-filter sequence. *MNRAS*, 442(4):3235–3242, 2014.
- G. E. Cook. Perturbations of near-circular orbits by the earth’s gravitational potential. *Planetary and Space Science*, 14(5):433–444, 1966.
- R. A. Cook. The long-term behavior of near-circular orbits in a zonal gravity field. *Advances in the Astronautical Sciences*, 76:2205–2221, 1992.
- D. Cox, J. Little, and D. O’Shea. *Ideals, Varieties, and Algorithms*. Springer-Verlag, 1992.
- D. Escobar, A. Águeda, L. Martín, and F. M. Martínez. Efficient all vs. all collision risk analyses. *Journal of Aerospace Engineering, Sciences and Applications*, 4(2):40–48, 2012.
- G. F. Gronchi. On the stationary points of the squared distance between two ellipses with a common focus. *SIAM Journal on Scientific Computing*, 24(1):61–80, 2003.
- G. F. Gronchi. An algebraic method to compute the critical points of the distance function between two keplerian orbits. *Celestial Mechanics and Dynamical Astronomy*, 93:295–329, 2005.
- G. F. Gronchi, G. Baù, and C. Grassi. Revisiting the computation of the critical points of the keplerian distance. *Celestial Mechanics and Dynamical Astronomy*, 135(5):48, 2023.
- L. M. Healy. Close conjunction detection on parallel computer. *Journal of Guidance, Control, and Dynamics*, 18(4):824–829, 1995.

- J. M. Hedo, M. Ruíz, and J. Peláez. On the minimum orbital intersection distance computation: a new effective method. *MNRAS*, 479(3):3288–3299, 2018.
- J. M. Hedo, E. Fantino, M. Ruíz, and J. Peláez. Minimum orbital intersection distance: an asymptotic approach. *A&A*, 633:A22, 2020.
- F. R. Hoots, L. L. Crawford, and R. L. Roehrich. An analytic method to determine future close approaches between satellites. *Celestial Mechanics*, 33(2):143–158, 1984.
- W. M. Kaula. *Theory of Satellite Geodesy: Applications of Satellites to Geodesy*. Blaisdell Publishing Company, 1966.
- E. Kerr and N. Sánchez Ortiz. State of the art and future needs in conjunction analysis methods, processes and software. In *Proceedings of the 8th European Conference on Space Debris (virtual), Darmstadt, Germany, 20–23 April 2021*, 2021.
- Z. N. Khutorovsky, V. F. Boikov, and S. Y. Kamensky. Direct method for the analysis of collision probability of artificial space objects in leo: techniques, results and applications. In *Proceedings of the First European Conference on Space Debris, Darmstadt, Germany, 5-7 April 1993*, pages 491–508, 1993.
- Y. Kozai. The motion of a close earth satellite. *The Astronomical Journal*, 64:367–377, 1959.
- Y. Kozai. Second-order solution of artificial satellite theory without air drag. *The Astronomical Journal*, 67(7):446–461, 1962.
- R. H. Lyddane. Small eccentricities or inclinations in the brouwer theory of the artificial satellite. *The Astronomical Journal*, 68(8):555–558, 1963.
- T. J. Muelhaupt, E. S. Marlon, J. Morin, and R. S. Wilson. Space traffic management in the new space era. *Journal of Space Safety Engineering*, 6(2):80–87, 2019.
- Ana S. Rivero, Claudio Bombardelli, and Rafael Vazquez. Short-term space occupancy and conjunction filter, 2024. URL <https://arxiv.org/abs/2309.02379>.
- W. M Smart. *Celestial Mechanics*. Longmans, Green & Co, 1953.
- E. Stevenson, V. Rodriguez-Fernandez, H. Urrutxua, and D. Camacho. Benchmarking deep learning approaches for all-vs-all conjunction screening. *Advances in Space Research*, 72(7):2660–2675, 2023.
- D. A Vallado, P. Crawford, R. Hujsak, and T. S. Kelso. Revisiting spacetrack report# 3: Rev 1. In *AIAA/AAS Astrodynamics Specialist Conference and Exhibit, 21-24 August 2006, Keystone, CO*, 2006.
- J. Woodburn, V. Coppola, and F. Stoner. A description of filters for minimizing the time required for orbital conjunction computations. *Advances in the Astronautical Sciences*, 135:1157–1173, 2010.

A Polynomial coefficients

For convenience, let us introduce

$$\sigma = \sqrt{\frac{\kappa_\eta}{\kappa_\xi}}, \quad K = \frac{J_2}{4\hat{a}}, \quad \kappa = \sin^2 \hat{l}.$$

The coefficients of the polynomial $q(x)$, introduced in (25), are given by:

$$q_0 = \frac{\hat{a}}{4} \left[4e_f(e_f^2 - 1) - 2e_f e_p^2(2 - 3\sigma^2) + 8e_f e_p \cos \beta_* \right. \\ \left. - 2e_f e_p^2(2 + 3\sigma^2) \cos 2\beta_* - e_p \sigma(4 - 12e_f^2 - e_p^2(2 - 3\sigma^2)) \sin \beta_* + 4e_p^2 \sigma \sin 2\beta_* - e_p^3 \sigma(2 + \sigma^2) \sin 3\beta_* \right],$$

$$q_1 = 2\hat{a} [2e_f^2 - e_p^2(1 - \sigma^2)] - 8K\kappa - \frac{1}{2}\hat{a}e_p [28e_f^2 \\ + e_p^2(7\sigma^2 - 6) - 4] \cos \beta_* - 2\hat{a}e_p^2(1 + \sigma^2) \cos 2\beta_* \\ + \hat{a}e_p^3 \left(1 + \frac{7}{2}\sigma^2\right) \cos 3\beta_* + 2\hat{a}e_f e_p \sigma(4 \sin \beta_* - 7e_p \sin 2\beta_*),$$

$$q_2 = -\frac{\hat{a}}{4} \left[4e_f(1 + 11e_f^2) - 2e_f e_p^2(34 - 33\sigma^2) + 40e_f e_p \cos \beta_* \right. \\ \left. - 2e_f e_p^2(34 + 33\sigma^2) \cos 2\beta_* + e_p \sigma(4 + 132e_f^2 - e_p^2(34 - 33\sigma^2)) \sin \beta_* + 20e_p^2 \sigma \sin 2\beta_* - e_p^3 \sigma(34 + 11\sigma^2) \sin 3\beta_* \right],$$

$$q_3 = 2\hat{a}e_p \cos \beta_* \left[2 + 22e_f^2 - e_p^2(4 - 11\sigma^2) \right. \\ \left. - e_p^2(4 + 11\sigma^2) \cos 2\beta_* + 44e_f e_p \sigma \sin \beta_* \right]$$

$$q_4 = \frac{\hat{a}}{4} \left[4e_f(1 + 11e_f^2) - 2e_f e_p^2(34 - 33\sigma^2) - 40e_f e_p \cos \beta_* \right. \\ \left. - 2e_f e_p^2(34 + 33\sigma^2) \cos 2\beta_* + e_p \sigma(4 + 132e_f^2 - e_p^2(34 - 33\sigma^2)) \sin \beta_* - 20e_p^2 \sigma \sin 2\beta_* - e_p^3 \sigma(34 + 11\sigma^2) \sin 3\beta_* \right],$$

$$q_5 = 2\hat{a} [e_p^2(1 - \sigma^2) - 2e_f^2] + 8K\kappa - \frac{1}{2}\hat{a}e_p [28e_f^2 \\ + e_p^2(7\sigma^2 - 6) - 4] \cos \beta_* + 2\hat{a}e_p^2(1 + \sigma^2) \cos 2\beta_* \\ + \hat{a}e_p^3 \left(1 + \frac{7}{2}\sigma^2\right) \cos 3\beta_* - 2\hat{a}e_f e_p \sigma(4 \sin \beta_* + 7e_p \sin 2\beta_*),$$

$$q_6 = -\frac{\hat{a}}{4} \left[4e_f(e_f^2 - 1) - 2e_f e_p^2(2 - 3\sigma^2) - 8e_f e_p \cos \beta_* \right. \\ \left. - 2e_f e_p^2(2 + 3\sigma^2) \cos 2\beta_* - e_p \sigma(4 - 12e_f^2 + e_p^2(2 - 3\sigma^2)) \sin \beta_* - 4e_p^2 \sigma \sin 2\beta_* - e_p^3 \sigma(2 + \sigma^2) \sin 3\beta_* \right].$$

The coefficients of the polynomial $p(y)$, introduced in (25), are given by:

$$p_0 = \frac{\sigma}{4} \left[-4e_f + 2e_f e_p \cos \hat{\theta}_* - 4e_f \cos 2\hat{\theta}_* + 6e_f e_p \cos 3\hat{\theta}_* \right. \\ \left. - (4 - 3e_f^2 - e_p^2) \sin \hat{\theta}_* + 4e_p \sin 2\hat{\theta}_* + 3(e_f^2 - e_p^2) \sin 3\hat{\theta}_* \right],$$

$$p_1 = \frac{1}{2} \left[4e_p(1 - \sigma^2) + (4 - e_f^2 + e_p^2(2\sigma^2 - 3)) \cos \hat{\theta}_* \right. \\ \left. - 4e_p(1 + \sigma^2) \cos 2\hat{\theta}_* + 3(e_p^2(1 + 2\sigma^2) - e_f^2) \cos 3\hat{\theta}_* \right. \\ \left. - 2e_f e_p(1 - 3\sigma^2) \sin \hat{\theta}_* - 4e_f \sin 2\hat{\theta}_* \right. \\ \left. + 6e_f e_p(1 + \sigma^2) \sin 3\hat{\theta}_* \right],$$

$$p_2 = -\frac{\sigma}{4} \left[4e_f + 10e_f e_p \cos \hat{\theta}_* + 4e_f \cos 2\hat{\theta}_* + 30e_f e_p \cos 3\hat{\theta}_* \right. \\ \left. + (4 - 3e_f^2 + e_p^2(11 - 12\sigma^2)) \sin \hat{\theta}_* + 20e_p \sin 2\hat{\theta}_* \right. \\ \left. - 3(e_f^2 + e_p^2(11 + 4\sigma^2)) \sin 3\hat{\theta}_* \right],$$

$$p_3 = 2 \cos \hat{\theta}_* \left[2 + e_f^2 + e_p^2(3 + 4\sigma^2) - 3(e_f^2 + e_p^2(1 + 4\sigma^2)) \cos 2\hat{\theta}_* \right. \\ \left. - 4e_f \sin \hat{\theta}_* \right],$$

$$p_4 = \frac{\sigma}{4} \left[4e_f - 10e_f e_p \cos \hat{\theta}_* + 4e_f \cos 2\hat{\theta}_* - 30e_f e_p \cos 3\hat{\theta}_* \right. \\ \left. + (4 - 3e_f^2 + e_p^2(11 - 12\sigma^2)) \sin \hat{\theta}_* - 20e_p \sin 2\hat{\theta}_* \right. \\ \left. - 3(e_f^2 + e_p^2(11 + 4\sigma^2)) \sin 3\hat{\theta}_* \right],$$

$$p_5 = \frac{1}{2} \left[4e_p(\sigma^2 - 1) + (4 - e_f^2 + e_p^2(2\sigma^2 - 3)) \cos \hat{\theta}_* \right. \\ \left. + 4e_p(1 + \sigma^2) \cos 2\hat{\theta}_* + 3(e_p^2(1 + 2\sigma^2) - e_f^2) \cos 3\hat{\theta}_* \right. \\ \left. + 2e_f e_p(1 - 3\sigma^2) \sin \hat{\theta}_* - 4e_f \sin 2\hat{\theta}_* \right. \\ \left. - 6e_f e_p(1 + \sigma^2) \sin 3\hat{\theta}_* \right],$$

$$p_6 = \frac{\sigma}{4} \left[4e_f + 2e_f e_p \cos \hat{\theta}_* + 4e_f \cos 2\hat{\theta}_* + 6e_f e_p \cos 3\hat{\theta}_* \right. \\ \left. + (4 - 3e_f^2 - e_p^2) \sin \hat{\theta}_* + 4e_p \sin 2\hat{\theta}_* - 3(e_f^2 - e_p^2) \sin 3\hat{\theta}_* \right].$$

B Values of the angular and radial buffers

The values of the angular buffer depend on the mutual inclination of the pair and the orbit inclination \hat{i} of each object. Tables 6 and 7 report the values at the initial time t_0 and final time t_f , respectively.

The values of the radial buffer depend on the semi-major axis \hat{a} , eccentricity \hat{e} , and the precession period T_C of the apsidal line. Tables 8 and 9 report the values for $\hat{a} > 10,000$ km and $\hat{a} \leq 10,000$ km, respectively.

Mutual inclination (deg)	Orbit inclination (deg)														
	[0, 10]	(10, 20]	(20, 30]	(30, 40]	(40, 50]	(50, 60]	(60, 70]	(70, 80]	(80, 90]	(90, 100]	(100, 110]	(110, 120]	(120, 130]	(130, 140]	(140, 150]
[10, 15]	0.114	0.181	0.303	0.226	0.237	0.241	0.201	0.156	0.102	0.104	0.133	0.138	0.140	0	0.367
(15, 20]	0.175	0.158	0.323	0.176	0.221	0.158	0.140	0.107	0.083	0.092	0.093	0.097	0.125	0	0.130
(20, 25]	0.164	0.113	0.142	0.132	0.119	0.124	0.091	0.081	0.064	0.075	0.075	0.075	0.087	0	0.095
(25, 30]	0.107	0.086	0.158	0.111	0.096	0.099	0.082	0.064	0.053	0.059	0.069	0.060	0.067	0	0.097
(30, 35]	0.087	0.084	0.101	0.138	0.079	0.084	0.070	0.054	0.050	0.057	0.051	0.052	0.062	0	0.084
(35, 40]	0.102	0.080	0.090	0.093	0.072	0.075	0.059	0.050	0.045	0.042	0.045	0.041	0.045	0	0.067
(40, 45]	0.066	0.071	0.084	0.067	0.057	0.064	0.053	0.043	0.035	0.039	0.040	0.036	0.040	0	0.065
(45, 50]	0.071	0.065	0.074	0.064	0.054	0.059	0.045	0.038	0.033	0.035	0.034	0.034	0.034	0	0.052
(50, 55]	0.061	0.063	0.066	0.062	0.046	0.054	0.042	0.035	0.030	0.030	0.031	0.027	0.030	0	0.049
(55, 60]	0.065	0.059	0.084	0.057	0.044	0.049	0.038	0.034	0.026	0.028	0.029	0.025	0.031	0	0.047
(60, 65]	0.059	0.056	0.074	0.052	0.049	0.047	0.032	0.032	0.026	0.025	0.027	0.020	0.025	0	0.043
(65, 70]	0.057	0.055	0.076	0.048	0.050	0.044	0.033	0.029	0.026	0.026	0.026	0.023	0.026	0	0.044
(70, 75]	0.054	0.053	0.073	0.046	0.051	0.042	0.029	0.025	0.026	0.025	0.026	0.023	0.026	0	0.043
(75, 80]	0.049	0.052	0.053	0.046	0.043	0.041	0.030	0.024	0.026	0.025	0.022	0.020	0.027	0	0.043
(80, 85]	0.046	0.053	0.085	0.049	0.041	0.053	0.029	0.023	0.024	0.023	0.024	0.027	0.029	0	0.046
(85, 90]	0.044	0.049	0.056	0.049	0.040	0.041	0.031	0.024	0.022	0.024	0.025	0.030	0.034	0	0.045
(90, 95]	0.040	0.050	0.058	0.049	0.043	0.042	0.032	0.026	0.023	0.024	0.028	0.028	0.037	0	0.045
(95, 100]	0.037	0.050	0.053	0.049	0.045	0.044	0.038	0.027	0.024	0.026	0.028	0.027	0.039	0	0.046
(100, 105]	0	0.049	0.053	0.048	0.043	0.046	0.035	0.030	0.026	0.028	0.030	0.032	0.036	0	0.042
(105, 110]	0	0.047	0.052	0.049	0.044	0.047	0.040	0.030	0.027	0.030	0.032	0.034	0.037	0	0.042
(110, 115]	0	0	0.050	0.047	0.045	0.046	0.041	0.032	0.028	0.032	0.033	0.032	0.034	0	0.040
(115, 120]	0	0	0.049	0.046	0.045	0.047	0.043	0.033	0.029	0.034	0.037	0.039	0.033	0	0.039
(120, 125]	0	0	0	0.045	0.042	0.049	0.044	0.037	0.034	0.038	0.038	0.039	0.037	0	0.037
(125, 130]	0	0	0	0.044	0.042	0.050	0.052	0.039	0.037	0.040	0.042	0.039	0.034	0	0
(130, 135]	0	0	0	0	0.040	0.050	0.050	0.044	0.039	0.043	0.043	0.037	0.042	0	0
(135, 140]	0	0	0	0	0.036	0.049	0.050	0.048	0.039	0.046	0.043	0.037	0.043	0	0
(140, 145]	0	0	0	0	0	0.048	0.050	0.044	0.043	0.046	0.043	0.037	0.039	0	0
(145, 150]	0	0	0	0	0	0.039	0.050	0.045	0.045	0.045	0.044	0.037	0.030	0	0
(150, 155]	0	0	0	0	0	0	0.050	0.047	0.045	0.045	0.042	0.036	0	0	0
(155, 160]	0	0	0	0	0	0	0.047	0.046	0.057	0.053	0.051	0	0	0	0
(160, 165]	0	0	0	0	0	0	0	0.049	0.060	0.062	0.047	0	0	0	0
(165, 170]	0	0	0	0	0	0	0	0.042	0.052	0.062	0.044	0	0	0	0

Table 6: Values of the angular buffer (in degrees) at t_0 .

Mutual inclination (deg)	Orbit inclination (deg)														
	[0, 10]	(10, 20]	(20, 30]	(30, 40]	(40, 50]	(50, 60]	(60, 70]	(70, 80]	(80, 90]	(90, 100]	(100, 110]	(110, 120]	(120, 130]	(130, 140]	(140, 150]
[10, 15]	0.253	0.305	0.387	0.363	0.339	0.294	0.332	0.331	0.249	0.316	0.309	0.285	0.232	0	0.240
(15, 20]	0.533	0.314	0.323	0.323	0.216	0.235	0.270	0.280	0.165	0.217	0.246	0.180	0.312	0	0.153
(20, 25]	0.530	0.298	0.311	0.267	0.177	0.195	0.203	0.124	0.131	0.183	0.162	0.144	0.150	0	0.123
(25, 30]	0.461	0.298	0.282	0.223	0.139	0.189	0.151	0.105	0.124	0.138	0.154	0.096	0.144	0	0.121
(30, 35]	0.388	0.292	0.261	0.192	0.136	0.165	0.119	0.092	0.082	0.133	0.119	0.071	0.100	0	0.086
(35, 40]	0.385	0.303	0.219	0.179	0.124	0.127	0.104	0.096	0.078	0.094	0.082	0.061	0.074	0	0.112
(40, 45]	0.327	0.279	0.199	0.164	0.107	0.108	0.089	0.089	0.066	0.075	0.069	0.055	0.067	0	0.093
(45, 50]	0.317	0.275	0.206	0.149	0.091	0.087	0.083	0.085	0.065	0.058	0.056	0.041	0.059	0	0.094
(50, 55]	0.339	0.256	0.182	0.125	0.084	0.075	0.069	0.074	0.066	0.052	0.052	0.037	0.054	0	0.085
(55, 60]	0.331	0.234	0.168	0.107	0.069	0.069	0.063	0.062	0.063	0.049	0.047	0.031	0.057	0	0.078
(60, 65]	0.320	0.221	0.165	0.108	0.068	0.076	0.052	0.052	0.058	0.049	0.046	0.036	0.052	0	0.078
(65, 70]	0.319	0.218	0.146	0.103	0.078	0.067	0.048	0.041	0.055	0.048	0.036	0.034	0.058	0	0.068
(70, 75]	0.311	0.209	0.142	0.097	0.066	0.068	0.056	0.038	0.052	0.045	0.038	0.045	0.047	0	0.066
(75, 80]	0.308	0.202	0.143	0.099	0.064	0.071	0.058	0.048	0.034	0.036	0.043	0.042	0.053	0	0.059
(80, 85]	0.298	0.206	0.144	0.107	0.063	0.073	0.064	0.051	0.040	0.038	0.045	0.044	0.053	0	0.058
(85, 90]	0.285	0.202	0.146	0.099	0.068	0.091	0.065	0.056	0.046	0.042	0.049	0.047	0.077	0	0.064
(90, 95]	0.274	0.199	0.138	0.107	0.077	0.099	0.065	0.060	0.050	0.057	0.055	0.057	0.090	0	0.064
(95, 100]	0.231	0.197	0.139	0.104	0.074	0.088	0.062	0.060	0.053	0.056	0.064	0.062	0.081	0	0.068
(100, 105]	0	0.188	0.133	0.102	0.078	0.098	0.078	0.062	0.055	0.063	0.068	0.065	0.091	0	0.069
(105, 110]	0	0.112	0.129	0.100	0.085	0.097	0.074	0.058	0.057	0.072	0.077	0.066	0.056	0	0.075
(110, 115]	0	0	0.120	0.108	0.087	0.110	0.090	0.090	0.056	0.084	0.081	0.074	0.096	0	0.076
(115, 120]	0	0	0.101	0.092	0.093	0.110	0.096	0.091	0.062	0.085	0.090	0.078	0.100	0	0.073
(120, 125]	0	0	0	0.078	0.095	0.114	0.103	0.081	0.060	0.090	0.093	0.084	0.093	0	0.055
(125, 130]	0	0	0	0.038	0.092	0.123	0.112	0.088	0.083	0.098	0.099	0.091	0.094	0	0
(130, 135]	0	0	0	0	0.076	0.116	0.121	0.100	0.071	0.106	0.104	0.094	0.064	0	0
(135, 140]	0	0	0	0	0.072	0.095	0.126	0.111	0.085	0.114	0.107	0.093	0.091	0	0
(140, 145]	0	0	0	0	0	0.087	0.124	0.121	0.091	0.115	0.118	0.095	0.051	0	0
(145, 150]	0	0	0	0	0	0.064	0.123	0.136	0.107	0.132	0.126	0.090	0.031	0	0
(150, 155]	0	0	0	0	0	0	0.114	0.140	0.142	0.141	0.144	0.083	0	0	0
(155, 160]	0	0	0	0	0	0	0.100	0.139	0.157	0.158	0.146	0	0	0	0
(160, 165]	0	0	0	0	0	0	0	0.123	0.167	0.167	0.137	0	0	0	0
(165, 170]	0	0	0	0	0	0	0	0.122	0.173	0.174	0.129	0	0	0	0

Table 7: Values of the angular buffer (in degrees) at t_f .

Eccentricity	Apsidal line period (days)	
	(0, 350]	> 350
[0, 0.01]	0	2.154
(0.01, 0.02]	0	2.239
(0.02, 0.03]	0	2.445
(0.03, 0.04]	0	2.449
(0.04, 0.05]	0	2.412
(0.05, 0.06]	0	2.403
(0.06, 0.07]	0.497	0.510
(0.07, 0.08]	0.599	4.876
(0.08, 0.09]	0	0
(0.09, 0.1]	0	0

Table 8: Values of the radial buffer (in km) for $\hat{a} > 10,000$ km. All orbits in the dataset satisfying this condition on \hat{a} have $T_C > 300$ days.

Eccentricity	Apsidal line period (days)							
	(0, 50]	(50, 100]	(100, 150]	(150, 200]	(200, 250]	(250, 300]	(300, 350]	> 350
[0, 0.01]	1.093	1.078	0.752	0.719	0.603	0.580	0.679	0.752
(0.01, 0.02]	0.925	0.635	0.900	0.711	0.625	0.588	0.713	0.767
(0.02, 0.03]	1.089	0.733	0.848	0.667	0.516	0.635	0.367	0.855
(0.03, 0.04]	2.241	1.017	0.836	0.858	0.637	0.384	0	1.073
(0.04, 0.05]	2.436	1.113	0.878	0.670	0.936	0.639	0	1.161
(0.05, 0.06]	1.970	1.700	0.948	0.708	1.178	0	0	1.123
(0.06, 0.07]	2.805	1.969	1.066	0.964	1.160	0.577	1.147	1.362
(0.07, 0.08]	2.641	2.179	0.874	1.028	0.801	0.971	0.605	1.558
(0.08, 0.09]	3.730	2.535	1.067	0.808	0.752	1.369	0.680	1.636
(0.09, 0.1]	2.794	2.574	1.787	1.608	1.503	0	0	1.780

Table 9: Values of the radial buffer (in km) for $\hat{a} \leq 10,000$ km.